To the Graduate Council:

I am submitting herewith a thesis written by David Michael McCarthy entitled "The Elastic and Magnetic Properties of $Tb_6Fe(Sb,Bi)_2$ Using Resonant Ultrasound Spectroscopy" I have examined the final electronic copy of this thesis for form and content and recommend that it be accepted in partial fulfillment of the requirements for the degree of Masters of Science with a major in Materials Science and Engineering.

Veerle M. Keppens
Major Professor

We have read this thesis
and recommend its acceptance:

Easo P. George

Gerd Duscher

Accepted for the Council:

Carolyn R. Hodges
Vice Provost and
Dean of the Graduate School

(Original signatures are on file with official student records.

The Elastic and Magnetic Properties of $Tb_6Fe(Sb,Bi)_2$ Using Resonant Ultrasound Spectroscopy.

A Thesis Presented for the
Master of Science
Degree
The University of Tennessee, Knoxville

David M. McCarthy
August 2010

Copyright © 2010 by David M. McCarthy.
All rights reserved.

ACKNOWEDGEMENTS

I would like to express my appreciation for my colleagues Lin Jia and Michael Koehler for their ideas and discussion pertaining to my research. Also thanks to, Dr. Veerle Keppens, my advisor and professor, for the hard work in making this all possible. Whether it is funding or editing, proofing, and reviewing this thesis, she has been a tremendous help. I would also like to acknowledge my committee for their review and critique of this thesis. Thanks also to Kris Bronstad for reviewing the formatting and style of this thesis.

Finally, I would like to thank the Department of Defense for their funding and continued support of this project.

ABSTRACT

Tb_6FeSb_2 and Tb_6FeBi_2 are novel rare earth compounds with little prior research. These compounds show high and variable Curie temperatures for rare-earth compounds. This has lead to a literature review of these materials and theories such as: elasticity, resonance, and magnetism. This thesis discusses the theory and methodology which can relate these various properties to each other.

Synthesis, X-ray analysis, sample preparation, and resonant ultrasound spectroscopy of Tb_6FeSb_2 and Tb_6FeBi_2 were completed. Resonant ultrasound spectroscopy (RUS) elastic studies were conducted for Tb_6FeSb_2 and Tb_6FeBi_2 as a function temperature from 5-300K, in various magnetic fields ranging from 0-9T, yielding Tb_6FeSb_2's and Tb_6FeBi_2's elastic moduli as a function of temperature. Magnetization vs. field data of Tb_6FeX_2 (X= Sb or Bi) with temperature provides additional information for the magnetic properties.

Tb_6FeSb_2 and Tb_6FeBi_2 Curie temperatures are 253(3)K and 246(5)K respectively. The low temperature magnetic transition is found near 70K for Tb_6FeSb_2 and near 50K for Tb_6FeBi_2. RUS suggests that this low temperature transition is somehow related to a structural transition, although no structural transition is observed in these two compounds. Cobalt substitution of Tb_6FeX_2 on the iron site greatly affects this lower temperature transition, as seen by RUS. Co-substitution does not greatly affect the Curie temperature. Low temperature X-ray diffraction shows that Co-substitution promotes a structural transition in this family of compounds.

TABLE OF CONTENTS

Chapter Page

CHAPTER I
Introduction and General Information 1
CHAPTER II
Literature Review 3
$Tb_6Fe(Sb,Bi)_2$ 3
Elasticity 6
Acoustic Resonances 11
Acoustic Techniques 17
Resonant Ultrasound Spectroscopy Calculation 20
Practical Considerations 27
Phase transitions 28
Uses and Applications 30
Magnetism 31
Magnetic Domains 33
Rare Earth Magnets 35
Magnetic-Structural Transformations 36
CHAPTER III
Materials and Methods 38
Synthesis of Tb_6FeSb_2 and Tb_6FeBi_2 38
Physical Properties Measurement System 38
RUS Setup and Experimentation 41
CHAPTER IV
Results and Discussion 45
Structural Involvement 54
Magnetization 55
CHAPTER V
Future Work AND Conclusions 60
REFERENCES
LIST OF REFERENCES 63
APPENDIX
Vita 72

LIST OF TABLES

Table Page

APPENDIX
Table 1: Atomic and thermal parameters for Tb6FeSb2 compounds. (Cai 2006) .4
Table 2: The parity triplets resulting from three mirror planes.....27
Table 3: The bond lengths and number of nearest neighbors of each atom in Tb_6FeSb_2.....65

LIST OF FIGURES

Figure Page

Figure 1: Unit cell of the Zr6CoAs2-type compound and magnetic structure. (Morozkin 2004) 4
Figure 2: Magnetization (M) vs. Temperature with a field of 1 kilogaus for Tb_6FeSb_2 (Cai 2006) 5
Figure 3: The reciprocal of molar susceptibility (χ_m) vs Temperature for Tb_6FeSb_2. The data is linearly fit at high temperature to the Curie-Weiss law. (Cai 2006) 6
Figure 4: A simple oscillating system that produces uncertainties that are intrinsic to all acoustic resonances 13
Figure 5: The real, imaginary, and magnitude acoustic resonances. (Migliori 1997) 16
Figure 6: These are examples of acoustic resonance modes. Left is a pure shear mode. K=4 n=1. Right is a volume oscillation mode. K=5 n=1. (Migliori 1997) 16
Figure 7: Pulse Echo Ultrasound setup (A) and signal (B). (Pantea 2005) 18
Figure 8: A typical RUS spectrum showing several resonances. 19
Figure 9: Domains when a) magnetized and c) demagnetized. 34
Figure 10: Rotations of magnetic moments across domain walls. 35
Figure 11: An example of a structural-magnetic transition with large elastic strains. 37
Figure 12: The x-ray powder diffraction results of my synthesis of Tb_6FeSb_2. 39
Figure 13: The x-ray powder diffraction results of my synthesis of Tb_6FeBi_2. 39
Figure 14: A) The VSM is situated atop to the PPMS from Quantum Design. 40
Figure 15: Our custom designed RUS probe option. Samples are situated between the two silver transducers in the left image. 41
Figure 16: RUS electronics of the system used by our research group. 43
Figure 17: The typical RUS setup. 43
Figure 18: C_{11} of Tb_6FeBi_2 as a function of field and temperature. Error within 1% 46
Figure 19: C_{44} modulus of Tb_6FeBi_2 as a function of field and temperature. 46
Figure 20: Young's Modulus of Tb_6FeBi_2 as a function of field and temperature. 48
Figure 21: Poisson's ratio of Tb_6FeBi_2 as a function of temperature and field. 48
Figure 22: C_{44} of Tb_6FeSb_2 as a function of field and temperature. 49
Figure 23: C_{44} of Tb_6FeSb_2 near the Curie temperature. 50
Figure 24: C_{11} of Tb6FeSb2 as a function of field and temperature. 51
Figure 25: C_{11} of Tb6FeSb2 near the Curie temperature. 51
Figure 26: The Young's modulus of Tb_6FeSb_2 as a function of field and temperature. 52
Figure 27: Poisson's ratio for Tb_6FeSb_2 as a function of temperature and field. 53
Figure 28: Effects of Cobalt substitution on Tb_6FeBi_2 suggest structural changes. 54

Figure 29: Effects of Cobalt substitution on Tb_6FeSb_2 also suggest structural changes. 55
Figure 30: High temperature M v. H data for Tb_6FeSb_2. 56
Figure 31: High temperature M v. H data for Tb_6FeBi_2....56
Figure 32: Magnetization data of Tb_6FeBi_2 between 50-130K. 57
Figure 33: Magnetization data of Tb_6FeSb_2 between 50-130K. 58
Figure 34: Coercive Fields vs. Temperature of Tb_6FeSb_2 and Tb_6FeBi_2....59

CHAPTER I

INTRODUCTION AND GENERAL INFORMATION

The search for advanced magnetic materials has led our research group to look into newly synthesized magnetic compounds. We hope this leads to the characterization of new materials with novel properties. New magnetic materials may have applications in areas like: magnetic refrigeration, increased data storage capacity, superior magnetic sensors, enhanced thermoelectrics, improved actuators, and better transducers. Implementating these new magnetic materials is hindered by the inability to find materials which can operate near room temperature. The ongoing search for new materials is the only way to overcome some of these difficulties. This has spurred us on to conduct a search for new rare-earth magnetic compounds with higher Curie temperatures. Another thing that plagues current magnetic materials in applications is difficulty in manufacturing. This difficulty in manufacturing arises from the material properties like low toughness and hardness.

We believe that understanding the link between magnetism and elasticity will help us characterize materials which may fit the criteria for application. The elastic properties will provide information on how a material responds to strain. This information is important when it comes to machining the material into a part. In addition, elasticity provides insight into the fundamental interactions occurring within the material.

The temperature dependence of the elastic moduli also provides information about the structural nature of magnetic transitions. Magnetostriction exploits this link between elasticity and magnetism. Magnetostriction causes a material to exhibit a strain or a force when it is subjected to a magnetic field. This property is ubiquitous to a small

degree but it was not until the 1970s that “giant” magnetostriction was observed in Terbium, Dysprosium, and Iron alloys. These alloys proved unsuitable for many applications due to their inherent brittleness. Research was stalled as the scientific community shifted its study to piezoelectric materials offering similar strain/force properties, but interest has been revived based on evidence that magnetostrictive materials may produce strains/forces an order of magnitude larger than piezoelectrics. This evidence has inspired a new round of research from the Department of Defense.

Two promising candidates of interest are Tb_6FeX_2 with X=Bi, Sb. These compounds contain both iron and terbium; Iron and terbium alloys, like Terfenol-D are known to produce large magnetostrictions (Abbundi 1977). The possibly large magnetostriction of Tb_6FeX_2‘s (X=Sb, Bi) and its relatively high Curie temperature make this material attractive for study. These compounds were first synthesized in 2004 and attracted little research. The Tb_6FeX_2 system will be the first of many that will be examined in the course of this project.

This work reports Tb_6FeBi_2 and Tb_6FeSb_2’s elasticity and magnetization. These properties are related by various changes in by Resonant Ultrasound Spectroscopy (RUS). This study has been valuable as my group moves forward to making substitutions into Tb_6FeX_2 crystal structure. The constants of polycrystalline Tb_6FeBi_2 and Tb_6FeSb_2 are reported for the first time. Furthermore, magnetization data and new details about the magnetic transition and behavior at low temperatures are presented for review.

CHAPTER II

LITERATURE REVIEW

$Tb_6Fe(Sb,Bi)_2$

There has been very little previous research into the properties of $Tb_6Fe(Sb,Bi)_2$. Neutron diffraction studies on Tb_6FeBi_2 were first done by Morozkin et al. in 2004. Morozkin's data show that Tb_6FeBi_2 adopts a Zr_6CoAs_2 type structure with the space group P6b2m no. 189. Morozkin's neutron study was specifically designed to probe the magnetic structure of Tb_6FeBi_2. The results show that the terbium atoms carry the magnetic moment. Tb_6FeBi_2 was found to have a Curie temperature of 246K and shows a low temperature transition near 50K. Theories put forth suggest it is a magnetic transition from collinear ferromagnetism (FC) to non-collinear ferromagnetism (FNC) at 50(5)K.

Morozkin studied additional Zr_6CoAs_2-type compounds in 2005, particularly those containing holmium on the Zr site. Morozkin points out the large variability in the magnetic properties of Zr_6CoAs_2 type compounds. He specifically states substitution antimony on the As site resulting in slightly higher Curie temperature than bismuth. This paper is the first instance in the literature of Zr_6CoAs_2-type compounds with antimony fully substituting for bismuth. Furthermore, Morozin reports that the change in the transitional metal site can alter the Curie temperature by over 100K. The crystal unit cell is shown in Figure 1. The atom positions of Tb_6FeSb_2 are displayed in Table 1.

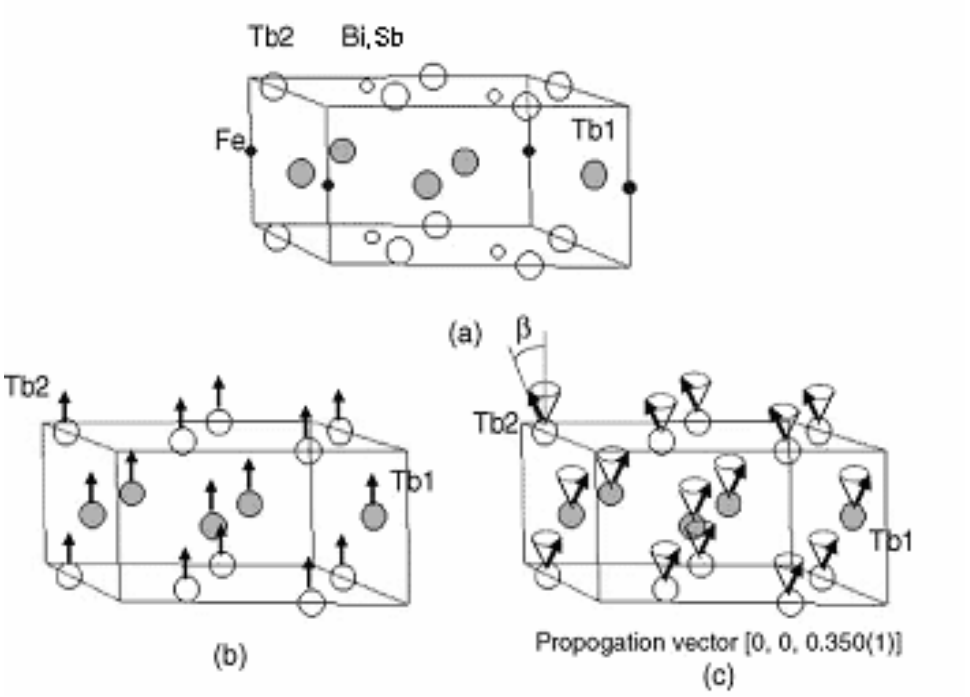


Figure 1: Unit cell of the Zr6CoAs2-type compound and magnetic structure (Morozkin 2004).

Table 1: Atomic and thermal parameters for Tb_6FeSb_2 compounds (Cai 2006).

Atom	Position	X	Y	Z	Occupancy	B_{eq} (Å^2)
Fe	1b	0	0	1/2	1	0.8(4)
Sb	2c	1/3	2/3	0	1	0.6(4)
Tb_1	3f	0.2376(2)	0	0	1	0.6(3)
Tb_2	3g	0.5978(2)	0	1/2	1	0.8(4)

Next, in 2006 G. Cai, J. Zhang, W. He, P. Qin, L. Zeng investigated Tb_6FeSb_2's magnetization from 85K to 400K and refined Tb_6FeSb_2 crystal structure via X-ray refinement. The bond lengths were also determined for Tb_6FeSb_2 in Table 3 in the appendix. The magnetization data from Cai's paper in 2006 is shown in Figure 2 and Figure 3 (Cai 2006). In 2007, Cai's group expanded their research to include Tb_6FeBi_2 and focused on the Curie transition range (220-290K). They reported a standard second-order Curie transition, soft magnetic behavior in the ferromagnetic range, magnetization vs. field data, and magnetic entropy for Tb_6FeBi_2 (He 2007).

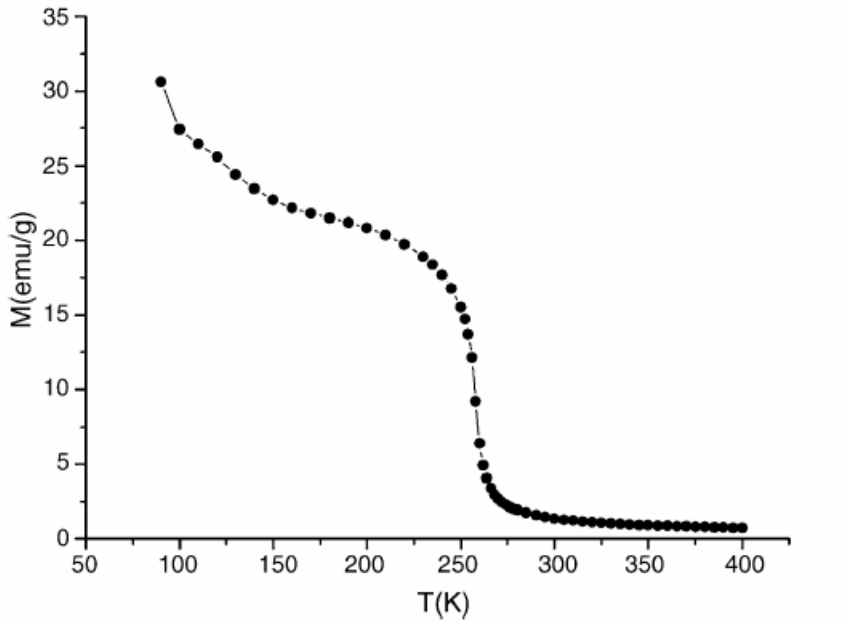


Figure 2: Magnetization (M) vs. Temperature with a field of 1 kilogaus for Tb_6FeSb_2 (Cai 2006)

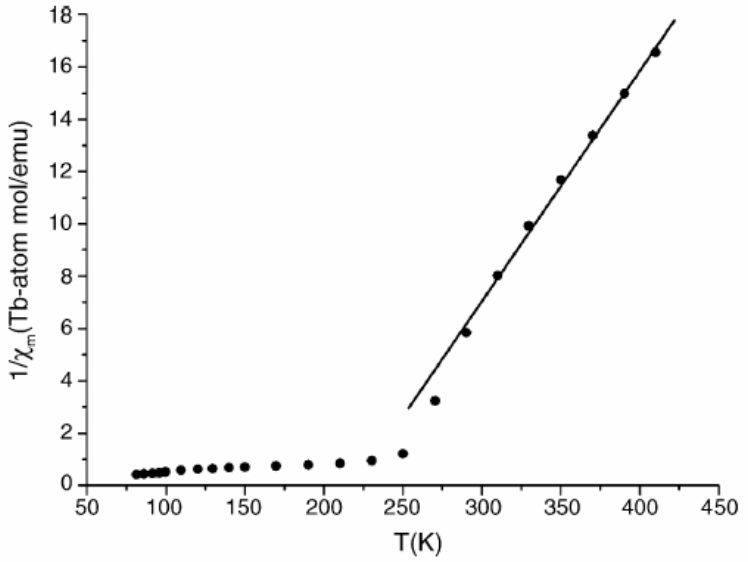


Figure 3: The reciprocal of molar susceptibility (χ_m) vs Temperature for Tb_6FeSb_2. The data is linearly fit at high temperature to the Curie-Weiss law (Cai 2006).

Elasticity

Elasticity was first modeled by Robert Hooke in 1660. Hooke postulated that materials behave in a spring-like fashion, prior to permanently deforming. He also modeled such behavior with respect to force. Hooke's law states that for small displacements, the force exerted by a material spring is linearly proportional to the displacement. Or stresses are directly proportional to strains by the elastic moduli in a given material. This law is the basis of elastic theory. This is the one dimensional case.

$$F = -kx \quad \textbf{(1)}$$

And

$$\sigma = E\varepsilon \quad \textbf{(2)}$$

k is the linear spring constant. x is the displacement. E is the Young's modulus (Pressure/strain). ε is the relative displacement also known as the strain. σ is the stress or Force/Area. Since the stress or pressure depends upon the area on which it acts, the development of elastic theory followed the development of the mathematics for describing areas and geometries. Elasticity theory is derived from matrix algebra, calculus, and differential equations.

First, elasticity is complex since sound/stress waves are not strictly longitudinal plane waves when they propagate. These waves contain parallel and perpendicular components, or rather longitudinal and shear components of stress and strain. These components likewise have longitudinal and shear moduli and are related to two independent sound velocities (Migliori 1997).

This can be seen when we consider that the inertial force of the atoms according to Newton's second law always balances the spring forces from Hooke's law in a given direction. After some derivation and integration, this balance can be rewritten simply as,

$$\frac{E}{\rho}\frac{d^2U}{dx^2} = \frac{d^2U}{dt^2} \quad \textbf{(3)}$$

U is a coordinate used to define the displacement vector of a strain. This differential equation may be solved using,

$$U(x,t) = U_0 e^{i(kx-\omega t)} \quad \textbf{(4)}$$

Furthermore, the inertial force depends upon the sound velocity, natural frequency, and density. Where the solution is,

$$\frac{\omega}{k} = \sqrt{\frac{E}{\rho}} = v_E \quad \textbf{(5)}$$

v_E is the young's modulus' sound velocity. ω is the natural resonance frequency. E is the young's modulus. k is the linear spring constant. This physical relation between elasticity, frequency, and sound velocity is important for acoustics.

Let us further consider the nature of displacements and strains. For multiple dimensions, we need to define arbitrary directions x, y, and z such that they are orthogonal to each other. Since strains may be parallel or perpendicular to their associated stresses, there are many permutations to denote different strains (Schreiber 1973). This requires a convention to define shear strains with respect to the perpendicular components such that,

$$\varepsilon_{xy} = \frac{\Delta U_x(i) - \Delta U_x(i-1)}{y(i) - y(i-1)} = \frac{\partial U_x^{new}(i)}{\partial y} \quad \textbf{(6)}$$

$$\varepsilon_{yx} = \frac{\Delta U_y(i) - \Delta U_y(i-1)}{x(i) - x(i-1)} = \frac{\partial U_y^{new}(i)}{\partial x} \quad \textbf{(7)}$$

Since x, y, and z are arbitrary, ε_{xy} and ε_{yx} are still not universally defined. Rotations of the coordinate system should not affect physical quantities, like experimentally measured strains. We must therefore define an invariant strain, not subject to coordinate rotation, by averaging to yield a quantity known as a principle strain (Migliori 1997).

$$\varepsilon_{12} = \frac{1}{2}\left(\frac{\partial U_1}{\partial x_2} + \frac{\partial U_2}{\partial x_1}\right) \quad \textbf{(8)}$$

The numbers 1,2, and 3 are substituted for the principle set of x, y, and z. (x_2 is equal to y.) This transformation can be applied to other indices as well. Let us return to Hooke's law. μ is one of Lamé coefficients which involve the shear modulus.

$$\sigma_{ij} = \mu\varepsilon_{ik}; \quad i \neq j \quad \textbf{(9)}$$

This consideration of rotational geometry and invariants lends itself to the use of matrix algebra. This relation in equation 9 can also be written as,

$$\begin{pmatrix} \sigma_{12} \\ \sigma_{13} \\ \sigma_{23} \end{pmatrix} = \begin{pmatrix} \mu & 0 & 0 \\ 0 & \mu & 0 \\ 0 & 0 & \mu \end{pmatrix} \begin{pmatrix} \varepsilon_{12} \\ \varepsilon_{13} \\ \varepsilon_{23} \end{pmatrix} \quad \textbf{(10)}$$

Now strains will cause out-of-plane stresses. An object will shrink or expand when subjected to an out-of-plane stress. Define the second Lamé coefficient, λ, such that the out of plane stresses are equal. This is shown below in equation 11 and 12.

$$\begin{pmatrix} \sigma_{11} \\ \sigma_{22} \\ \sigma_{33} \end{pmatrix} = \begin{pmatrix} c_{11} & \lambda & \lambda \\ \lambda & c_{11} & \lambda \\ \lambda & \lambda & c_{11} \end{pmatrix} \begin{pmatrix} \varepsilon_{11} \\ \varepsilon_{22} \\ \varepsilon_{33} \end{pmatrix} \quad \textbf{(11)}$$

or

$$\sigma_{22} = \sigma_{33} = \lambda\varepsilon_{11} \quad \textbf{(12)}$$

We can combine the strain and the stress matrices as follows to create equation 13. This adds some indeterminacy since λ and μ are not strictly defined. The sum of the eigenvalues yields one elastic modulus. Yet, this process can be used for each modulus.

$$c_{11} = \lambda + 2\mu \quad \textbf{(13)}$$

Nine different stresses and nine different strains may simultaneously exist in a material. However, mixed strains ε_{12} and ε_{21} are often physically similar. This reduces the problem to 6 stresses and 6 strains. (Rotation still requires 9x9 matrix.) Each Lamé and elastic constant would have four indices composed of two stress and two strain directions. For simplicity, it is beneficial to allow one number to represent the stress and one the strain as follows,

$$11 \to 1 \quad 22 \to 2 \quad 3 \to 33$$
$$23 \to 4 \quad 13 \to 5 \quad 12 \to 6$$

$$\begin{pmatrix} \sigma_1 \\ \sigma_2 \\ \sigma_3 \\ \sigma_4 \\ \sigma_5 \\ \sigma_6 \end{pmatrix} = \begin{pmatrix} c_{11} & c_{12} & c_{13} & c_{14} & c_{15} & c_{16} \\ c_{21} & c_{22} & c_{23} & c_{24} & c_{25} & c_{26} \\ c_{31} & c_{32} & c_{33} & c_{34} & c_{35} & c_{36} \\ c_{41} & c_{42} & c_{43} & c_{44} & c_{45} & c_{46} \\ c_{51} & c_{52} & c_{53} & c_{54} & c_{55} & c_{56} \\ c_{61} & c_{62} & c_{63} & c_{64} & c_{65} & c_{66} \end{pmatrix} \begin{pmatrix} \varepsilon_1 \\ \varepsilon_2 \\ \varepsilon_3 \\ \varepsilon_4 \\ \varepsilon_5 \\ \varepsilon_6 \end{pmatrix} \quad \textbf{(14)}$$

If we introduce symmetry on the crystallographic level, more constants are physically similar to each other. For a cubic system, there are three mirror planes across the x, y, and z. Thus Hooke's law becomes,

$$\begin{pmatrix} \sigma_1 \\ \sigma_2 \\ \sigma_3 \\ \sigma_4 \\ \sigma_5 \\ \sigma_6 \end{pmatrix} = \begin{pmatrix} c_{11} & c_{12} & c_{12} & 0 & 0 & 0 \\ c_{12} & c_{11} & c_{12} & 0 & 0 & 0 \\ c_{12} & c_{12} & c_{11} & 0 & 0 & 0 \\ 0 & 0 & 0 & c_{44} & 0 & 0 \\ 0 & 0 & 0 & 0 & c_{44} & 0 \\ 0 & 0 & 0 & 0 & 0 & c_{44} \end{pmatrix} \begin{pmatrix} \varepsilon_1 \\ \varepsilon_2 \\ \varepsilon_3 \\ \varepsilon_4 \\ \varepsilon_5 \\ \varepsilon_6 \end{pmatrix} \quad \textbf{(15)}$$

For an Isotropic system the symmetry reduces further since,

$$(c_{11} - c_{12})/2 = c_{44} \quad \textbf{(16)}$$

This leaves two independent moduli, c_{44} and c_{11}, corresponding to the shear and longitudinal directions. In addition, we may define dependant elastic moduli which are combinations of c_{44} and c_{11} that have physical significance. One modulus is the Young's modulus, E, which corresponds to tensile properties. Another modulus is the bulk modulus, which corresponds to volume compressibility.

$$E = \frac{\sigma_1}{\varepsilon_1} \quad and \quad B = \frac{\sigma_1}{\Delta V} = \frac{c_{11} + 2c_{12}}{3} \quad \textbf{(17)}$$

In conclusion, the large matrices involved in elasticity theory have limited its utility for real life applications. Fortunately, the computational challenges of elasticity have been met partially by computers, opening up the field to study.

Acoustic Resonances

Mechanical/acoustic resonances were first used as a tool in the early 19th century. Railroad workers would tap the steel wheels on trains and listen to timbre of the resonances. As a means of inspection, flawed or cracked wheels would produce distinct sets of resonances. Trained railroad workers would detect subtle differences in the sound and replace the wheel. These resonances accurately determined problems with the wheels (Migliori 1997). Scientists tried to understand and model the phenomena to no avail. Acoustics were not very well understood due to the difficulty in describing the geometry in which the resonances arose.

The first analytic solutions for calculating resonances of cubes and spheres came about in the 1880s by Gabriel Lamé and Horace Lamb. These solutions were for isotropic solids (Maynard 1996). The acoustic resonances were able to be calculated

given the elastic constants, mass, and dimensions. The mathematics for the inverse of finding elastic constants is not as direct. The ability to calculate elastic constants from observed resonances would be years away. There was little progress in this area until the invention of the modern computer in the 1970s.

With the computer, interest in acoustic resonances was revived in the geological community. Resonant ultrasound spectroscopy (RUS) was developed to analyze earthquakes though the earth. The sound velocities of our roughly spherical earth were slower than expected through the earth's mantel. This provided important evidence that the mantle is composed of molten liquid. Orson Anderson and Harold Demarest at AT&T Bell Labs advanced RUS in the geology community when they were confronted with analyzing millimeter sized samples (Maynard 1996). The small samples included glassy grains taken from earth's moon. Interestingly, the sound velocities for the lunar samples were equated to that of cheese (Schwarz 2000).

In 1976, Ichiro Ohno made significant extensions to Demarest's work, covering all the underlying principles of RUS. The expansion of RUS into other fields of science did not occur until Albert Migliori and Julian Maynard stumbled across it in 1988. Migliori and Maynard were investigating the elasticity of high-temperature cuprates. Upon a chance discovery of RUS in geological papers, Migliori made immediate improvements to the electronics and transducer design used. He also coined "Resonant Ultrasound Spectroscopy" to encompass the wide range of resonant techniques present in the geological community. Finally, William Visscher advanced RUS computer codes to their current level (Maynard 1996). RUS is still maturing as a technique and has yet to reach saturation in the sciences.

Acoustic resonance theory begins by applying Hooke's law to two equal masses attached together by a spring and a damper. A picture of this setup is shown in Figure 4. This simple system produces many of the same problems encountered in acoustic measurements. A major assumption regarding this system is that the sample is allowed to vibrate freely. This is a reasonable assumption for some techniques but not for others.

Let's begin by considering the forces in this system. There are inertial forces in the system for which Newton's second law applies,

$$F_{m1} = -m\frac{d^2x_1}{dt^2}, F_{m2} = -m\frac{d^2x_2}{dt^2} \quad \textbf{(18)}$$

x_2 and x_1 are the distances that these two masses travel from rest. Next, there are damping forces which resist inertial movement of the masses, with damping b.

$$F_{d1} = -b\frac{d(x_1 - x_2)}{dt}, F_{d2} = b\frac{d(x_1 - x_2)}{dt} \quad \textbf{(19)}$$

Finally, spring forces must be incorporated. They are modeled by Hooke's law.

$$F_{s1} = -k(x_1 - x_2), F_{s2} = k(x_1 - x_2) \quad \textbf{(20)}$$

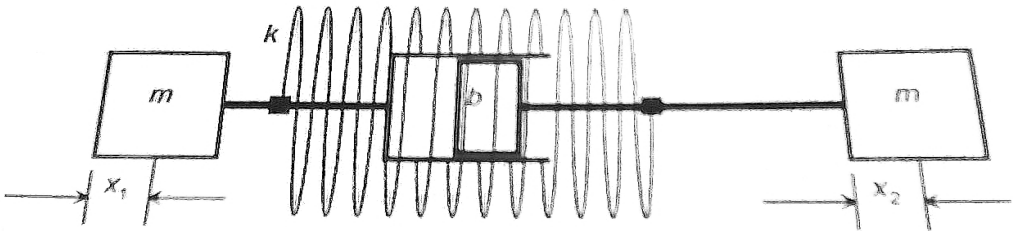


Figure 4: A simple oscillating system that produces uncertainties that are intrinsic to all acoustic resonances.

If all the forces are summed at one mass, the differential equation becomes,

$$-m\frac{d^2x}{dt^2} - 2b\frac{dx}{dt} - 2kx = 0 \quad \textbf{(21)}$$

Next, we may assume harmonic motion for the general solution to the system.

$$x(t) = x_0 e^{-i\omega t}, \ \ and \ \ \frac{d}{dt} \rightarrow -i\omega \ \ \ with \ \ \ \omega = 2\pi \mathrm{f} \quad \textbf{(22)}$$

When the general solution is applied to equation 21 the result is,

$$(\omega^2 m + 2i\omega b - 2k)x_0 e^{-i\omega t} = 0 \quad \textbf{(23)}$$

This indicates that the quantity in the parenthesis must equal zero. Using the quadratic equation, the roots for the solution are found for the frequency.

$$\omega = \pm\sqrt{\frac{2k}{m} - \left(\frac{b}{m}\right)^2} - \frac{ib}{m} \quad \textbf{(24)}$$

This allows us to define three important quantities: the natural frequency (ω_o) , the time constant (τ), and the number of cycles (Q).

$$\omega_0 = \sqrt{\frac{2k}{m}}, \ \ \tau = \frac{m}{b} \ \ and \ \ Q = \frac{\omega_0 \tau}{2} \quad \textbf{(25)}$$

The natural frequency is a resonance at which the system vibrates when unhindered. The time constant is used to determine decay of the vibration. The third parameter is the lifetime in number of cycles before the oscillator decays away.

Now in a system driven by an external force, the sums of forces is as follows,

$$-m\frac{d^2x}{dt^2} - 2b\frac{dx}{dt} - 2kx = Fe^{-i(\omega t-\pi/2)} \quad \textbf{(26)}$$

Using the prior definitions, we can define a solution for driven resonances as follows,

$$x(\omega,t) = x_0(\omega)e^{-i\omega t}, \quad with \quad x_0(\omega) = \frac{iFm^{-1}}{\omega^2 - \omega_0^2 + 2i\omega\omega_0 Q^{-1}} \quad \textbf{(27)}$$

This solution contains both real and imaginary components. The real component relates to the maximum force. The imaginary component relates to the maximum displacement. These two components are phase shifted by π/2. These components may have slightly different peak frequencies in a signal. Furthermore, a magnitude peak frequency is defined by both the real and imaginary components. These three resonant frequencies obscure the definition of resonances. Resonances could be defined in terms of force, displacement, or magnitude. In practice, one cannot easily distinguish these various components. The situation becomes much more difficult when the decaying cycles of a resonance overlap with another resonance mode. Figure 5 shows an example of how these resonances relate to each other (Migliori 1997). Some examples of resonant modes are shown in Figure 6.

Additional intrinsic errors are introduced when measuring sinusoidal waves regarding start and stop times of measured signals (Migliori 1997). There have been various algorithms developed to remove some ambiguity in evaluating the time dependant signals (Pantea 2005). These intrinsic errors are a constant source of error when it comes to measuring resonances. The magnitude of these errors in the grand scheme is negligible. The primary source of errors is within sample itself.

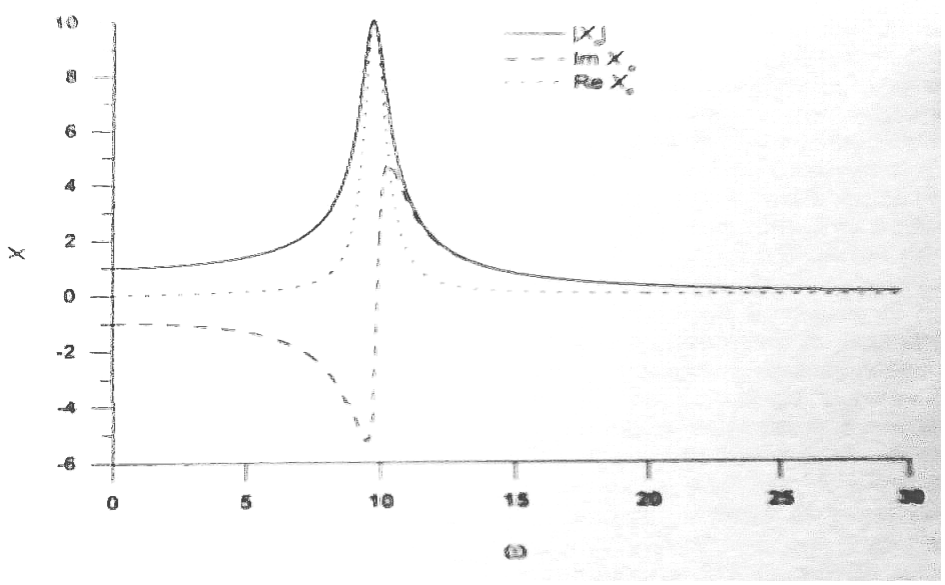


Figure 5: The real, imaginary, and magnitude acoustic resonances (Migliori 1997).

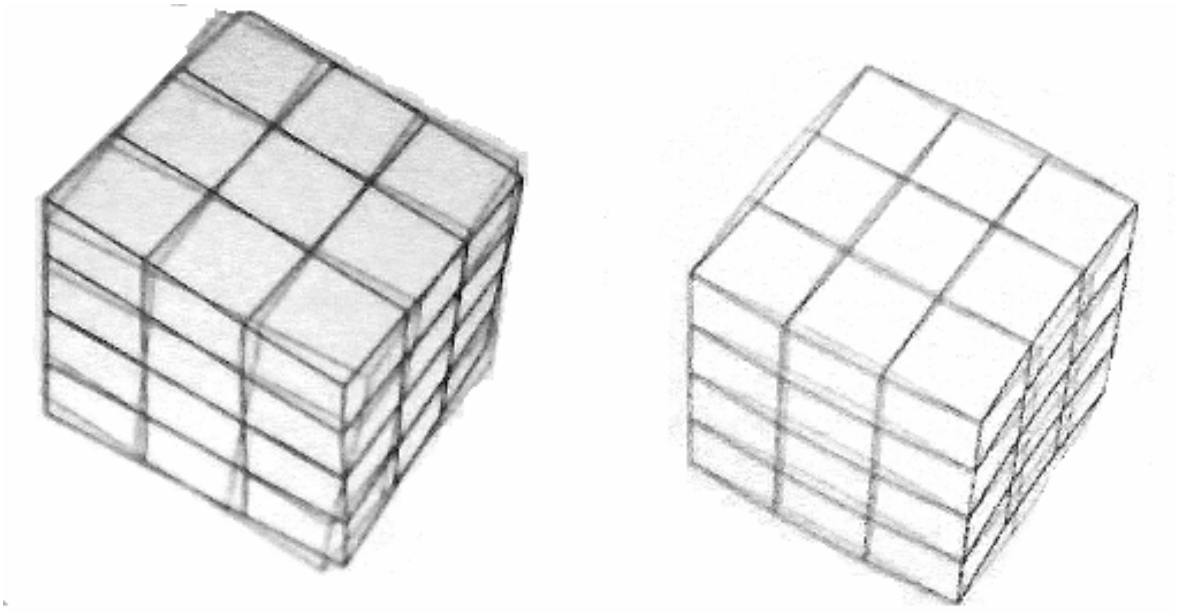


Figure 6: These are examples of acoustic resonance modes. Left is a pure shear mode. K=4 n=1. Right is a volume oscillation mode. K=5 n=1 (Migliori 1997).

Acoustic Techniques

There are two widely used ultrasound techniques used to characterize materials: Pulsed Echo Ultrasound and Resonant Ultrasound Spectroscopy (RUS). Pulsed Echo Ultrasound is a technique that uses a single excitation pulse to measure the sound velocity and attenuation in a single crystallographic direction. This technique requires two parallel sample faces. One face is attached to a piezoelectric transducer and/or a buffer rod with crystalbond wax. A pulse is sent across the sample. An echo is then received by the transducer. The time of transit is used to calculate the sound velocity. The sound velocity is proportional to the square of the elastic moduli as shown in equation 10 (Leisure 1997). The typical setup of Pulsed Echo Ultrasound and signal (as a function of time) is shown in Figure 7.

Pulsed echo ultrasound has its advantages and drawbacks. First, the physical bond of the transducer is known to strain the sample. This strain in the sample produces uncertain results, especially near phase transitions (Leisure 1997). Flaws in the sample also have a large effect on the quality of the measurement. The errors are additive since they slow the sound velocity. Pulsed Echo Ultrasound can only measure one sound velocity, thus elastic constant at a time. For materials with many elastic constants, the sample must be crystallographically aligned to a new direction after each measurement. Occasionally, these directions require measurements along non-principle crystallographic directions (Schwarz 2000). This is a time consuming process. It creates experimental complexity but greatly simplifies the computation of the elastic constants (Migliori 2005).

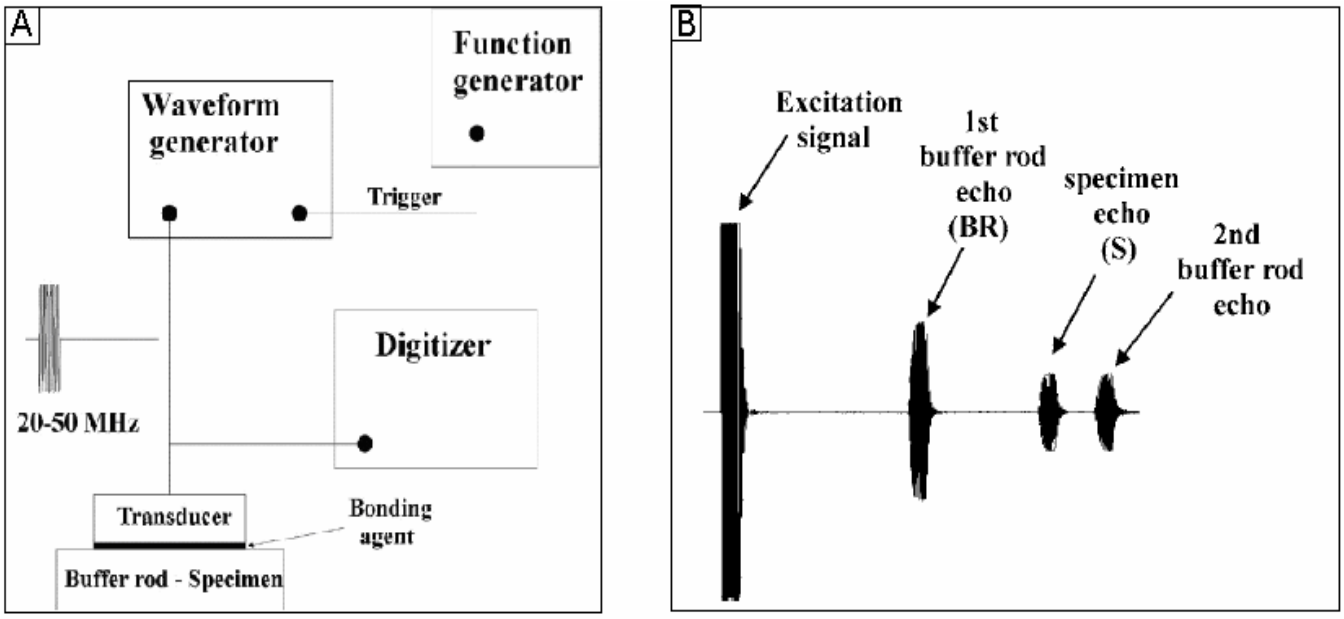


Figure 7: Pulse Echo Ultrasound setup (A) and signal (B). (Pantea 2005)

Resonant Ultrasound Spectroscopy (RUS) is another acoustic technique which makes use of whole body resonances. RUS consists of the continuous excitation of a freely vibrating sample with a known geometry. The sample is loosely situated between two transducers. One transducer converts an electrical signal into an acoustical signal while the other transducer measures the response. The frequency is then swept. The resulting signal is filtered, amplified, measured, and digitized.

The in-phase and out-of-phase components of the signal are measured and form a frequency spectrum. A typical RUS signal is shown in Figure 8. RUS is equivalent to measuring the resonant response function of the material (Migliori 1997). RUS errors are averaged over the volume of the sample (Schwarz 2000).

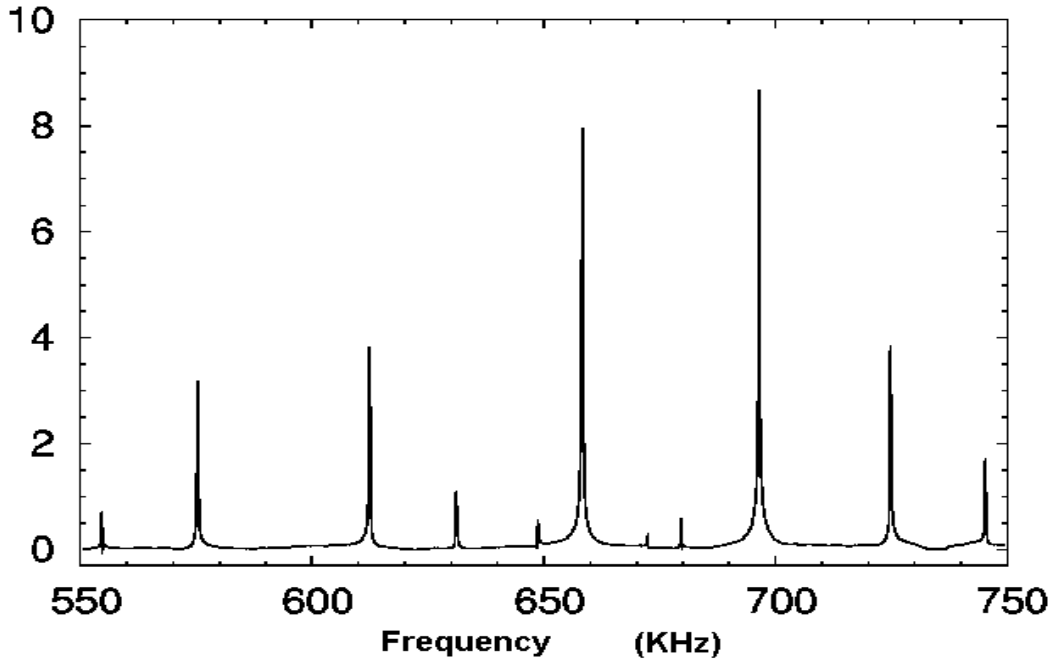


Figure 8: A typical RUS spectrum showing several resonances.

One problem with RUS is that mathematically complex solutions and codes to analyze RUS data are only available for a handful of geometries. These geometries include spheres, cylinders, and rectangular parallelepipeds (Schwarz 2000). Major errors primarily arise from sample preparation. Cumulative errors in well-prepared RUS samples are relatively small. A single RUS measurement will accurately yield the complete elastic tensor of a material, within 2% of the absolute value (Migliori 1997). RUS has the added advantage of working with millimeter sized samples (Schwarz 2000).

RUS has many advantages but they come at the expense of computational complexity. Unlike Pulsed echo ultrasound, RUS calculations are near impossible to do by hand since it requires manipulating a 9x9 matrix. This calculation of elastic constants does not depend on an oscilloscope but rather the raw power of iteration (Migliori 1997).

RUS is usually limited to modeling systems with orthorhombic or greater symmetry (Leisure 1997). RUS is not a fully automated process and requires a lot of human input. Migliori writes, “Unfortunately, both experience and good initial guesses of elastic moduli are still important for consistent success, in using even these well tested and frequently used codes to analyze RUS data” (Migliori 2005). This will become apparent when we discuss the calculation and analysis of data for RUS.

Resonant Ultrasound Spectroscopy Calculation

A resonant ultrasound spectrum is not a unique fingerprint. Many approximate fits are possible since several multiple variables go into the direct calculation. As we observed earlier, a sum of eigenvalues is used to find a solution to an elastic constant. Many eigenvalues can be added together to result in the same sum. The multitude of eigenvalues possible yields an indeterminacy which makes the calculation of elastic constants in RUS less straightforward.

There are two primary calculations in RUS. The calculation of resonances from the elastic constants is known as the “direct problem. The calculation of elastic constants from resonances is called the “inverse problem.” These two calculations require the shape and mass of the sample (Migliori 1997). The ‘inverse problem’ can only be solved statistically by calculating the ‘direct problem’ several times. First, an initial guess is supplied for the elastic constants then the resonances are calculated by the direct problem. These calculated resonances then are compared to the observed resonances. A goodness of fit algorithm is computed and minimized. Material

parameters, like the elastic constants, are iterated several times to calculate resonances that best account for the observed resonances (Migliori 1997).

This comparison between calculated and observed resonances requires every principle resonance, starting with the lowest, to be accounted for. If an observed resonance mode is missed, the best fit solution bears little resemblance to the actual resonances and the elastic constants will diverge from their true values. Thus, no resonance mode can be unknowingly missed in the analysis of the data (Migliori 2005),

The method of iteration of the elastic constants is very complex. Let's start by considering it in depth. This section roughly follows Albert Migliori's book Resonant Ultrasound Spectroscopy written in 1997.

First, there is equilibrium energy to each resonance. The lagrangian is the kinetic energy (KE) and potential energy (PE) in the system. Thus the lagrangian, L, must be minimized for the resonances.

$$L = \int_V (KE - PE) dV \quad \textbf{(28)}$$

KE is expressed as follows with 'u' relating to the displacement vector of the arbitrarily shaped solid. 'i' corresponds to the x, y, and z in coordinate space.

$$KE = \frac{1}{2} \sum_i \rho \omega^2 u_i^2 \quad \textbf{(29)}$$

PE is expressed as,

$$PE = \frac{1}{2} \sum_{i,j,k,l} c_{ijkl} \frac{\partial u_i}{\partial x_j} \frac{\partial u_k}{\partial x_l} \quad \textbf{(30)}$$

Now that the Lagrangian is defined, we assume harmonic oscillation of the position about u, with known time dependence. Keeping with first order only terms,

$$\delta L = \int_V \left[\sum_i \rho\omega^2 u_i \delta u_i - \sum_{i,j,k,l} c_{ijkl} \frac{\partial(\delta u_i)}{\partial x_j} \frac{\partial u_k}{\partial x_l} \right] dV \quad \textbf{(31)}$$

This can be integrated by parts yielding a surface integral.

$$\delta L = \int_V \left[\sum_i \rho\omega^2 u_i - \sum_{i,j,k,l} c_{ijkl} \frac{\partial^2 u_k}{\partial x_j \partial x_l} \right] dV - \int_S \left(\sum_i \left[\sum_{j,k,l} \vec{n}_j c_{ijkl} \frac{\partial u_k}{\partial x_l} \right] \delta u_i \right) dS \quad \textbf{(32)}$$

Since u is arbitrary on V and S, u_i can be set to values of stationary points such that KE=0. The elastic wave and free surface boundary equations result from this constraint,

$$\rho\omega^2 u_i + \sum_{j,k,l} c_{ijkl} \frac{\partial^2 u_k}{\partial x_j \partial x_l} = 0 \textbf{ and } \sum_{j,k,l} \vec{n}_j c_{ijkl} \frac{\partial u_k}{\partial x_l} = \sum_j \vec{n}_j \sigma_{ij} = 0 \quad \textbf{(33)}$$

Consequentially, u_i as thus defined can be described by the Rayleigh-Ritz method.

$$u_i = \sum_\lambda a_{i\lambda} \Phi_\lambda \quad \textbf{(34)}$$

Φ_λ is the complete set of functions which the displacement vectors expand into. This function is called the basis function. We may apply the function to Cartesian space,

$$\Phi_\lambda = x^l y^m z^n \quad \textbf{(35)}$$

λ is a label for a set of three non-negative integers.

Substituting the basis function into the Lagrangian,

$$\delta L = \int_V \frac{1}{2} \left[\sum_{i,i',\lambda,\lambda'} \delta_{ii'} \rho\omega^2 a_{i\lambda} a_{i'\lambda'} \Phi_\lambda \Phi_{\lambda'} - \sum_{i,j,k,l,\lambda,\lambda'} c_{ijkl} a_{i\lambda} a_{i'\lambda'} \frac{\partial \Phi_\lambda}{\partial x_j} \frac{\partial \Phi_{\lambda'}}{\partial x_l} \right] dV \quad \textbf{(36)}$$

λ and λ' are summations from 1 to N, where N < (l+m+n). This can be written in matrix notation as follows in equation 37.

$$L = \frac{1}{2}\omega^2 \vec{a}^T \ddot{E}\vec{a} - \frac{1}{2}\vec{a}^T \ddot{\Gamma}\vec{a} \quad \textbf{(37)}$$

E and Γ are matrices with order R. The number, R, is defined by this series. N is the order of the fitting polynomial.

$$R = 3(N+1)(N+2)(N+3).../3 \quad with \quad N \to \infty \quad \textbf{(38)}$$

This provides the exact solution. Albert Migliori writes this about N, "In practice, N must be restricted so as to give a good compromise between computational accuracy and computing time/memory requirements" (Migliori 1997, p38). This is the same indeterminacy that arises from calculating the eigenvalues discussed in the elasticity section. Only so many sets of eigenvalues are readily accounted for. Calculation errors decrease with increasing N. For most cases N is restricted to around N=10 to balance accuracy and computational resources. Sample errors tend to dominate over calculation errors beyond this level. The eigenvalue equation is as follows.

$$\omega^2 \ddot{E}\vec{a} = \ddot{\Gamma}\vec{a} \quad \textbf{(39)}$$

The derivative of the eigenvalue equation can be taken with respect to a sample parameter (p) such as an angle between the sample face and the crystallographic axes, a physical dimension, or an elastic constant. The result can be shown as,

$$\frac{\partial \omega^2}{\partial p} = \vec{a}^T \left[\frac{\partial \ddot{\Gamma}}{\partial p} - \omega^2 \frac{\partial \ddot{E}}{\partial p} \right] \vec{a} \quad \textbf{(40)}$$

This is true for every material and geometry. The derivative can be used to help direct the process of iteration.

The minimization of difference between the observed and the calculated frequencies requires defining a figure of merit.

$$F = \sum_{i=1}^{N} w_i (f_i - g_i)^2 \quad \textbf{(41)}$$

This goodness of fit equation is known as Levenberg-Marquardt's Algorithm (Migliori 1997). If a resonance frequency is known but not visible in the background of the signal, it can be weighted to zero to account for a missed mode. The figure of merit is also a useful measure of the accuracy of the indirect solution. The difference between a good fit and a fit with a missing mode is an order of magnitude or so (Migliori 2005). The figure of merit provides a reasonable assurance that the solution has validity.

The figure of merit equation is also used to arrive at the solution of that inverse problem. The figure of merit is first expanded into a Taylor series in equation 42. The vector x is composed of the elements of the expansion, with M dimensions. Also, the Taylor series requires an initial guess, x_o; it will slightly change the outcome.

$$F(\vec{x}) = F(\vec{x}_o) + \sum_{\alpha} (\vec{x} - \vec{x}_o)_\alpha \frac{\partial F(\vec{x}_o)}{\partial x_\alpha} + \sum_{\alpha,\beta} \frac{1}{2} (\vec{x} - \vec{x}_o)_\alpha \frac{\partial^2 F(\vec{x}_o)}{\partial x_\alpha \partial x_\beta} (\vec{x} - \vec{x}_o)_\beta \quad \textbf{(42)}$$

The fit equation holds true for small differences between x and x_o.

$$\vec{x} = \{x_a\} \text{ and } \alpha = 1...M \quad (43)$$

A rough estimate is generally sufficient. We continue by realizing that F is a minimum near the solution.

$$\frac{\partial F(\vec{x})}{\partial x_\alpha} = 0 \quad \textbf{(44)}$$

Implying,

$$\frac{\partial F(\vec{x})}{\partial x_\alpha} + \sum_\beta \frac{\partial^2 F(\vec{x}_o)}{\partial x_\alpha \partial x_\beta} (\vec{x} - \vec{x}_o)_\beta = 0 \quad \textbf{(45)}$$

This equation is essentially Newton's Method in M dimensions if solved for x. The first order derivative can be written explicitly as,

$$\frac{\partial F}{\partial x_\alpha} = \sum_i 2 w_i (f_i - g_i) \frac{\partial f_i}{\partial x_\alpha} \quad \textbf{(46)}$$

We may set equation 46 and equation 40 equal to each other since they both define derivatives of the material parameters. We arrive at,

$$\frac{\partial \omega_i}{\partial x_\alpha} = \frac{1}{2} \omega_i \frac{\partial \omega_i^2}{\partial x_\alpha} = \frac{1}{2} \omega_i \bullet \vec{a}^T \left[\frac{\partial \vec{\vec{\Gamma}}}{\partial x_\alpha} - \omega^2 \frac{\partial \vec{\vec{E}}}{\partial x_\alpha} \right] \vec{a} \quad \textbf{(47)}$$

This allows us to refine a material parameter such as the dimensions and the elastic constants. Now we must discuss conventions used to describe symmetry.

If there are three mirror planes in the system perpendicular to each other, the eight translations may be expressed as a parity triplet [-ξ,μ,ν] defined as $[(-1)^l,(-1)^m,(-1)^n]$ with l,m,n corresponding to x, y, and z. Each element in the parity triplet consists of a positive or negative sign. These signs denote the various mirror plane translations. These conditions are met by rectangular parallelepipeds, spheres, and cylinders.

If three mirror planes exist in the solid so that parity triplets describe the system, the calculation can be simplified. The diagonalization of the 1000x1000 element matrix

(with N=10) is reduced to eight 100x100 matrices. These result in large computational savings.

This convention also helps when discussing harmonic displacements since (-ξ,μ,ν) corresponds to actual directions in the sample. Each resonance has a displacement mode k. 'k' is defined by the parity triplet. When k=1, the parity triplet (–(+),+,+) denotes a translation across the x-direction. Likewise, k=2 (-(+),+,-) is equivalent to a rotation about the y-axis. Triplet parities help define different resonances with different displacements. The various triplet parities are shown in Table 2.

The parity triplets also govern the interactions between resonances. Resonances are in similar symmetry classes, if the resonance displacements are not perpendicular to each other. They are not perpendicular when adding the two parity triplets together yields something other than zero. Furthermore if two resonances are in similar symmetry classes, they will interact strongly as they approach each other in frequency (Migliori 2005). This is significant because resonant frequencies have different temperature dependencies. Frequencies may cross each other with changes in temperature (Migliori 1997).

Resonance modes that have nodes at corners or run parallel to the transducers are occasionally missed. Each resonance also has a fundamental harmonic 'i'. The displacement mode and fundamental harmonic, when combined, fully describe the physical motion of the resonances.

Table 2: The parity triplets resulting from three mirror planes

K	1	2	3	4	5	6	7	8
-ξ	+	+	+	+	-	-	-	-
μ	+	+	-	-	+	+	-	-
N	+	-	+	-	+	-	+	-
Mode	X-translation	Y-rotation	Z-rotation	Pure Shear	Pure Volume	Z-translation	Y-translation	X-rotation

Practical Considerations

A single-pulse system and Fourier transforms could be employed instead for RUS, but this has many disadvantages. The power per unit bandwidth would be very low, leading to excessive noise. If drive power was increased substantially to compensate for this effect, the sample would quite easily shift or become dislodged. Furthermore, when measuring the response, the bandwidth channels would have to be a lot larger to cover the whole frequency range. RUS instead generally sweeps frequencies with time via continuous sine wave excitation. The only disadvantage of this configuration is spending several seconds or minutes per scan (Migliori 1996).

Further consideration of the basis functions indicates that the calculation involves the explicit evaluation of the “geometric” integral. This simplifies tabulating the complete matrix elements in Γ and E. The geometric integral for a rectangular parallelepiped (RP) with sides $2d_1$, $2d_2$, and $2d_3$ is as follows,

$$f(p,q,r) = \int_V x^p y^q z^r dV = \frac{8 d_1^{p+1} d_2^{q+1} d_3^{r+1}}{(p+1)(q+1)(r+1)} \quad \textbf{(48)}$$

Geometry selection is a balance between ease of calculation and sample preparation. Experience has shown that parallelepipeds work best because other geometries like cubes, cylinders, and spheres also show degenerate or overlapping resonant modes (Schwarz 2000). Overlapping modes make analysis difficult since one must properly account for all the resonances. The typical number of resonances needed for calculating the elastic constants is at least 15 modes in isotropic systems and at least 40 modes in orthorhombic systems (Migliori 2005).

To implement the minimization of the fit equation, the various terms can be manipulated mathematically such that the derivatives are more easily defined. This allows for quicker solving of material parameters. The second order terms are usually ignored. The second order terms do not have an effect on defining the minimum. Their importance arises once a good fit is achieved; the curvatures of F (second order terms) with respect to different material parameters (c11, c12, c44, etc.) let us estimate the certainty of those parameters in the fit (Migliori 1997).

Phase transitions

RUS can examine electronic, magnetic, and crystallographic phase transitions. It will also pick up changes in phonon behavior. Elasticity has many links to thermodynamics. Pressure is the same unit as stress within a material. Volume changes may be thought of as an induced strain in the material. These two thermodynamic variables of volume and pressure have large contributions to determining free energy of

a system. Some elastic constants like the bulk modulus (B) can be found through thermodynamic means.

$$\frac{\partial^2 \Delta G}{\partial P^2} = \frac{\partial \Delta V}{\partial P} = -\frac{1}{B} \quad \textbf{(49)}$$

The free energy of the phase transformation contains terms involving the strain, the structural ordering parameter, and the coupling between the two. Using Landau's theory with a single strain and single component ordering parameter, the free energy formula is,

$$F = \frac{1}{2} c_0 \varepsilon^2 + \left[\frac{1}{2} \alpha (T - T_c) q^2 + \frac{1}{4} \beta q^4 \right] + \frac{1}{2} \gamma \varepsilon q^2 \quad \textbf{(50)}$$

Where q is the ordering parameter, α, β, c_0, and γ are temperature independent constants. The first term is the elastic energy. The second term is related to the energy of the ordering parameter in the transition. The last term is the coupling between the strain and the ordering parameter. The free energy of these three terms is continuous in material transitions. It is the abrupt change in last term that has an effect on elasticity measurements.

The nature of this strain-ordering coupling for phase transitions is complex. The largest effects arise from structural transitions. Superconducting transitions are usually very subtle. Only free energy is continuous in material transitions (Migliori 1997). For magnetic materials, there is coupling between the magnetic spins of electrons with the alignment of the electronic orbitals. This is known as spin-orbit coupling. the electronic orbitals exert forces on each other. These forces are the result of quantum exclusion principles and electrostatic charges. Thus, changes in electronic states may alter

change the orbit-orbit coupling. Over long distances, these effects result in orbit-lattice coupling. These changes, though small, are detected by RUS's high precision.

Finally, phonons, which are directional vibrations of atoms, control the movement of sound and heat through a material. Phonon scattering behaviors are observed indirectly in RUS though the attenuation of the ultrasound in the material. In RUS, this attenuation translates into broader peaks and larger Q values. Attenuation can be caused by many things: dislocations, point defects, interstitial atoms, substitution atoms, thermal phonons, strain-order parameter coupling, conduction electrons, atomic instabilities, magnetic/electric fields, and elastic dipoles. These all contribute to changes in phonon behavior. Phonon modes may soften near phase transitions leading to greater attenuation, even if the material does not undergo that transition (Migliori 1997).

Uses and Applications

RUS has many applications outside of the laboratory. RUS is very dependent upon shape and sample quality. This means small changes in density, size, shape, or sample cracks produce noticeable shifts in resonant frequencies. Only a few resonant frequencies need to be statistically compared to each other for differences in quality are noticed. RUS here plays a qualitative instead of quantitative role. This is a large advantage when it comes to non-destructive testing of various parts. The RUS scan may be quickly conducted on each part and then compared to a standardized spectrum for irregularities. It is common practice in developing and evaluating ball bearings (Schwarz 2000). RUS can also be used to detect cracking in bridges. Small cracks are easily picked up in RUS since they decrease the sound velocity in the material. If the

cracks are detected early, the bridge can be repaired before the cracks result in failure (Schwarz 2000).

Magnetism

One of the principle properties of an electron is its magnetic spin. The magnetic spin was first thought to arise from the orientation of quantized orbital angular momentum, but Dirac showed that it arose instead from quantum relativistic effects. The magnetic spin of an electron is denoted by the quantum number, m_s, which adopt half-integer values of positive +1/2 or negative -1/2. Electrons with various magnetic spins each have an amount of energy associated with them in an atom.

Atoms minimize their energy by filling their electronic orbitals in a particular order. Pauli's exclusion principle states each orbital can only hold two electrons with unique sets of quantum numbers, thus magnetic spins. Furthemore Hund's rule states all the equipotential orbitals in a sub-shell are filled with electrons parallel down spins (-1/2) first, then the down spins electrons are paired up with up spin electrons (+1/2).

In magnetic fields, the magnetic spin of the electron gives rises to a magnetic moment. If a down spin electron is not cancelled in an orbital by an up spin electron in an atom, this produces a magnetic moment in the atom (Spaldin 2003). These magnetic moments may contain angular momentum. Nicola Spaldin writes, "the orbital angular momentum vector can never point directly along the direction of the field…instead it precesses in a cone around the field direction, like a gyroscope tipped off its axis." (Spaldin 2003, p26).

Magnetic moments in solidsgive rise to four main classes of materials. These four classes all depend on the magnetic susceptibility of the material. If the moments are randomly orientated, the material is said to be paramagnetic. If the moments are aligned parallel to each other, the material is said to be ferromagnetic. If the moments are aligned anti-parallel, the material is said to be anti-ferromagnetic. If the moments are aligned anti-parallel but one moment is larger than the other, the material is said to be ferrimagnetic. There are other magnetic states in which the magnetic moments rotate around an axis with a given angle.

Magnetic susceptibility gives rise to these classes as defined by the Curie-Weiss' law. Paramagnets that follow this law undergo spontaneous ordering below a critical temperature. Below this critical temperature, known as the Curie temperature, they are no longer paramagnetic. Curie postulated that the susceptibility of a paramagnet is inversely proportional to the temperature. Weiss refined Curie's law to include the notion that the magnetic susceptibility is directly proportional to the strength of this molecular field. We now know that the molecular field is actually not a field; it is the net result of mutual interactions and quantum mechanics. Curie-Weiss' law is written out below. χ is the magnetic susceptibility, M is the magnetization, H is the magnetizing field, C is a constant, T is temperature, and T_c is the Curie temperature.

$$\chi = \frac{M}{H} = \frac{C}{T - T_c} \quad \text{with } C = Nm^2 / 3k_B \quad \textbf{(51)}$$

Ferromagnetism can also be induced by the conduction band in paramagnetic metals. Iron is a common example of a paramagnetic metal that can be magnetized. An external magnetic field will energetically favor electronic states with magnetic spins of

one direction, near the Fermi level, over another in the metal. This allows the metal to pick up a net magnetization along the field direction (Spaldin 2003).

In addition, ferromagnetic materials can be classified in another way. If the magnet reverts completely to a paramagnetic or demagnetized state after the field is removed, the material is considered a soft magnet. If the material does not revert but shows hysteresis, the material is considered a hard magnet. The amount of magnetization remaining, after the field is removed, is the coercivity of the magnet. Magnetic coercivity occurs within material which for a variety of reasons. Reasons can include magnetostatic energy, magnetic crystalline anisotropy, magnetostrictive energy, and the intersection of domain walls with defects (Spaldin 2003).

Magnetic Domains

Magnetic domains are areas within a ferromagnet that have parallel magnetic moments. Spaldin writes this about domains, “When a ferromagnetic material is in its demagnetized state, the magnetization vectors in different domains have different orientations, and the total magnetization averages to zero. The process of magnetization causes all the domains to orient in the same direction” (Spaldin 2003, pg 73). Domain formation is driven by the energy balance of magnetostatic energy and spin-exchange interactions of the magnet. In zero field or coercive field, the energy goes into aligning the domains so that the material’s external magnetic flux is minimized. In magnetic field, external magnetic flux is ignored and exchange energy interactions are decreased. Spaldin writes, “When the field is applied, the domain whose magnetization is closest to the field starts to grow at the expense of the other

domains. The growth occurs by domain wall motion" (Spaldin 2003, pg 81). Domain formation is shown in Figure 9. The triangular domains near the surface of the material are known as domains of closure.

Domain walls favor spin rotations of 90° and 180°. These walls are the most energetically favorable since electrons aren't subject to demagnetizing fields of adjacent atom. The 90° tilt and the 180° twist boundaries are favored since magnetic moments remain perpendicular to each other across atoms in the domain wall. These rotations are shown in Figure 10.

The type of domain wall largely is dependant on what is favorable in the material. Some materials exhibit magnetic anisotropy. This causes spins of an "easy axis" direction to be favored over intermediate spins or "hard axis" directions. The magnetizations of easy and hard axes follow crystallographic directions. This affects the structure of domain walls formed by favoring 90° tilts. Furthermore, the energy difference between the material's easy and hard directions is called the magnetocrystalline anisotropy energy. Like exchange energy, the magnetocrystalline anisotropy energy encourages the growth of large domains and few domain boundaries (Spaldin 2003).

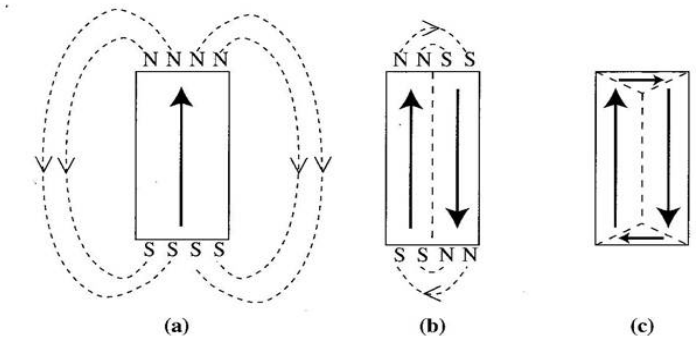


Figure 9: Domains when a) magnetized and c) demagnetized.

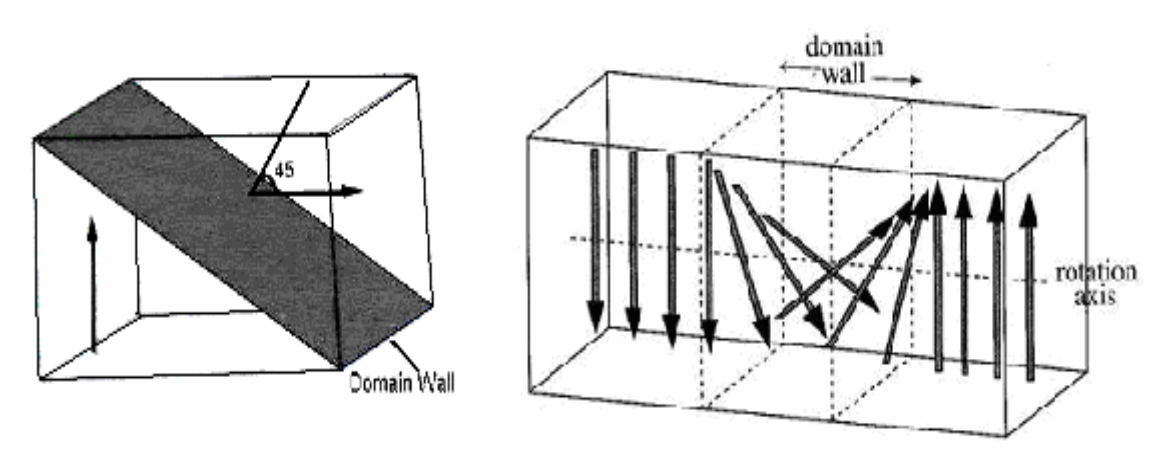


Figure 10: Rotations of magnetic moments across domain walls.

The magnetocrystalline anisotropy energy is directly related to the strength of the spin-orbit coupling. The spin-orbit coupling is the relation between the electron's magnetic moment and the atom's electronic orbital, in which the electron resides. This coupling will affect domain formation. Spaldin writes, "The energy required to rotate the spin system of a domain away from the easy axis is actually just the energy required to overcome the spin-orbit coupling. When an applied field tries to reorient the direction of the magnetic moment, the orbit also needs to be reoriented. However the orbit is in general also strongly coupled to the lattice, and so the attempt to rotate the spin axis is resisted" (Spaldin 2003, pg 124).

Rare Earth Magnets

The spin-orbit coupling is increased in materials with rare earth magnetic species. Rare-earth magnets show properties which other magnets do not. A large spin-orbit coupling yields larger magnetic coercivities. Rare earths valance electrons reside

in the f-shell orbitals which are more directional than d, s, and p sub-shells. This causes unpaired orbital's motion to be more strongly coupled to the electron's spin.

This spin-orbit coupling also gives rise to magnetostriction as orbitals rotate and interact with each other. Spaldin writes, "When a ferromagnetic material is magnetized it undergoes a change in length known as its magnetostriction… In iron, magnetostriction causes the triangular domains of closure to try to elongate horizontally, whereas the long vertical domains try to elongate vertically… Clearly the horizontal and vertical domains can't elongate at the same time, and instead an elastic strain term is added to the total energy" (Spaldin 2003, pg 78). Magnetostriction may also be negative resulting in contraction at the domain walls. Magnetostriction is often larger in rare earth materials due to their unique orbitals. Elasticity and magnetostriction are intuitively involved with each other in the process of magnetic ordering as we saw earlier.

Another thing unique to rare earths is longer range magnetization. Rare earth metals and alloys with non metallic species may contain magnetic ions that are too far apart to interact directly. They may however interact via conduction electrons. The magnetic ion polarizes its surrounding conduction electrons. The conduction electrons are delocalized and may result in the polarization of a distant second' magnetic ion. This is known as RKKY magnetization.

Magnetic-Structural Transformations

Magnetostriction arises from other processes like magnetic-structural transformations. These transformations are often coupled to changes in the easy axis (Spaldin 2003). This magnetic change can be understood by examining the dynamics of

phase transformations. One example is the FCC-BCT transformation which also produces large strains. The <100> direction in Face Centered Cubic (FCC) corresponds to <110> direction in Body Centered Tetragonal (BCT) system. The easy axis usually follows the <100> direction in BCT. This transformation is shown in Figure 11.

Coupled structure-magnetic transitions may produce energy barriers to the other transformation. A structural transition may spontaneously cause a magnetic transition from one easy axis to another axis, or a magnetic transition from one easy axis to the new easy axis may precede a structural change (Spaldin 2003). Structural transformations often contain their own strain terms which may or may not be affected by the strains already present via the domains.

Magnetically-coupled transitions often involve two transitions or a simultaneous transition at very close temperatures. These coupled transitions may be favored or suppressed by external magnetic fields. Sometimes, only one of the two transitions is suppressed in the material. The effects of the suppressed transition may still be seen on the lattice via changes in the equation (50) of the strain-order free energy balance.

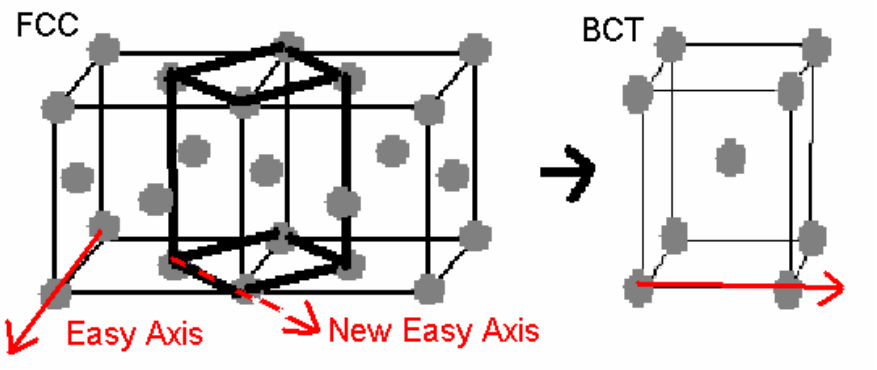


Figure 11: An example of a structural-magnetic transition with large elastic strains.

CHAPTER III
MATERIALS AND METHODS

Synthesis of Tb_6FeSb_2 and Tb_6FeBi_2

Tb, Fe, Bi, and Sb metals were measured into stochiometric amounts for each sample with 2% excess bismuth or 1% excess antimony. The elemental metals were melted and mixed together in an arc melter, wrapped in tantalum foil, and encapsulated in silica glass tubes under an argon vacuum, then placed into tube furnaces and annealed. Several attempts at synthesis were made. The results are from two Tb_6FeSb_6 samples, which were annealed at 1150K for 168h and ice water quenched, and the one Tb_6FeBi_2 sample, annealed at 1100K for 168h and ice water quenched. A small piece was cut from each sample and prepared for x-ray powder diffraction. The three viable samples were cut and formed into parallelepipeds and finely polished for RUS. The XRD results are shown in Figure 12 and Figure 13. Tb_6FeSb_2 hexagonal lattice constants are a=4.180Å and c=8.182Å, while Tb_6FeBi_2 are a=4.201Å and c=8.287Å.

Physical Properties Measurement System

The Physical Properties Measurements System (PPMS) developed by Quantum Design is a cryogenic system with a temperature range of 1.9K to 400K. It contains a superconducting magnet that can reach 9T. The PPMS is used to measure temperature and magnetic dependence properties. The system is able to accommodate many different options for various measurements.

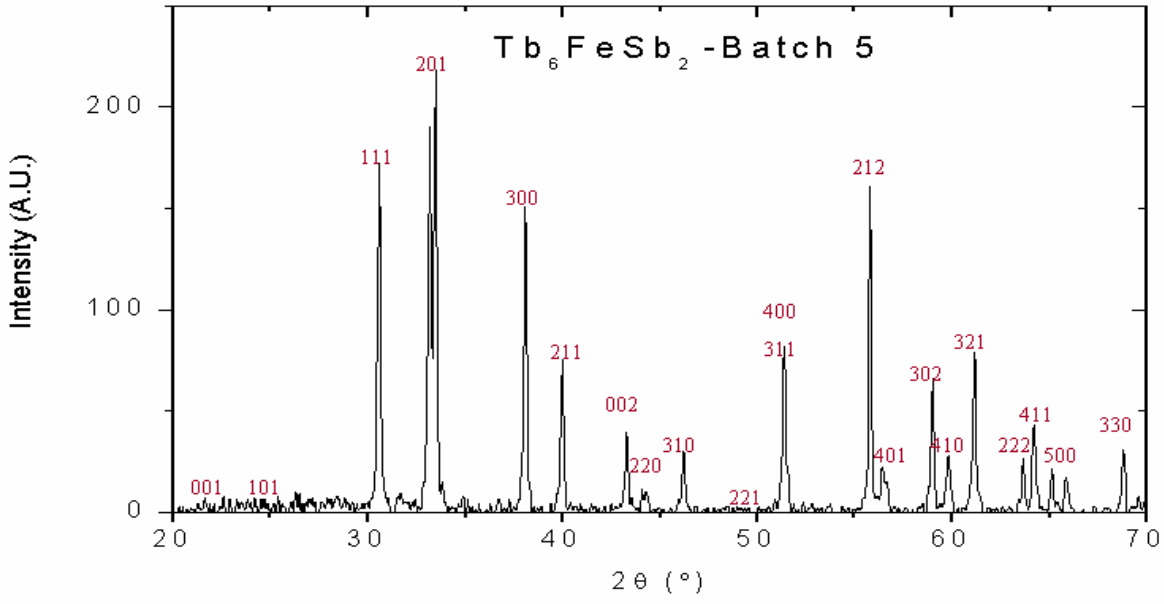


Figure 12: The x-ray powder diffraction results of my synthesis of Tb_6FeSb_2.

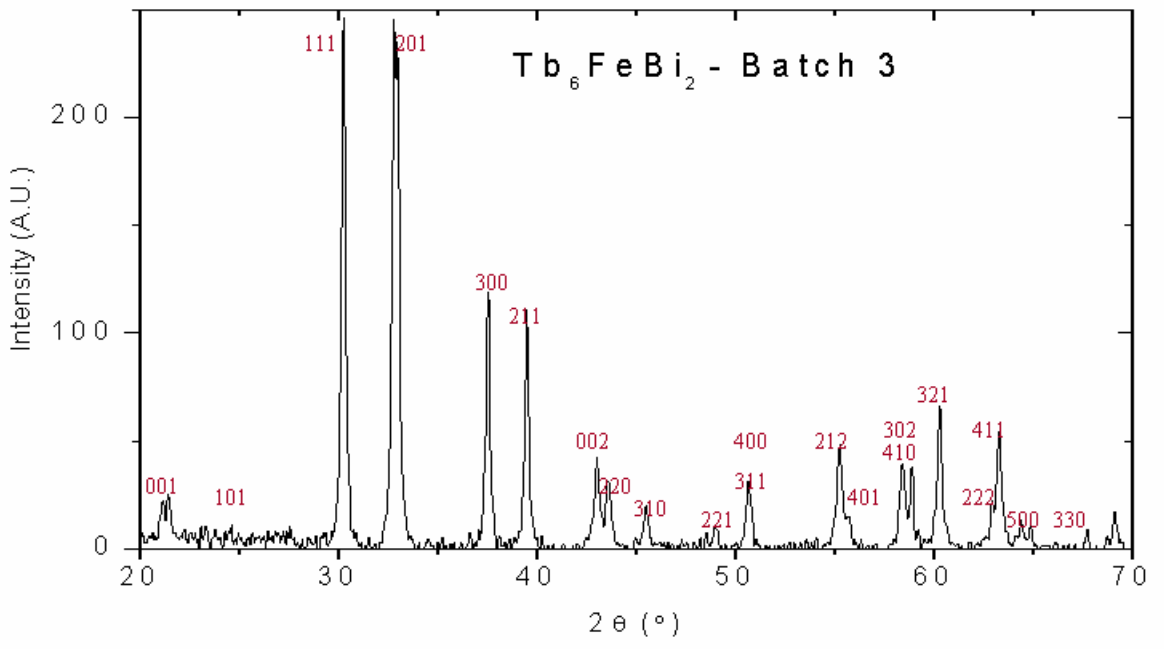


Figure 13: The x-ray powder diffraction results of my synthesis of Tb_6FeBi_2.

The Standard PPMS option used in this study is the Vibrating Sample Magnetometer (VSM). The VSM measures the magnetic behavior of materials. The basic principle of the VSM is Faraday's law of Induction.

$$|\varepsilon| = \left| \frac{d\Phi_B}{dt} \right| \quad \textbf{(52)}$$

Magnetization fields may be applied to the sample in the VSM. As the magnetized sample vibrates, its magnetic field induces electromotive forces, ε, in the coil set. These electromotive forces create alternating currents that are proportional to the sample's magnetic flux and velocity of the sample. Once calibrated, the magnetization of a sample can be obtained. The VSM option of the PPMS is shown below in Figure 14.

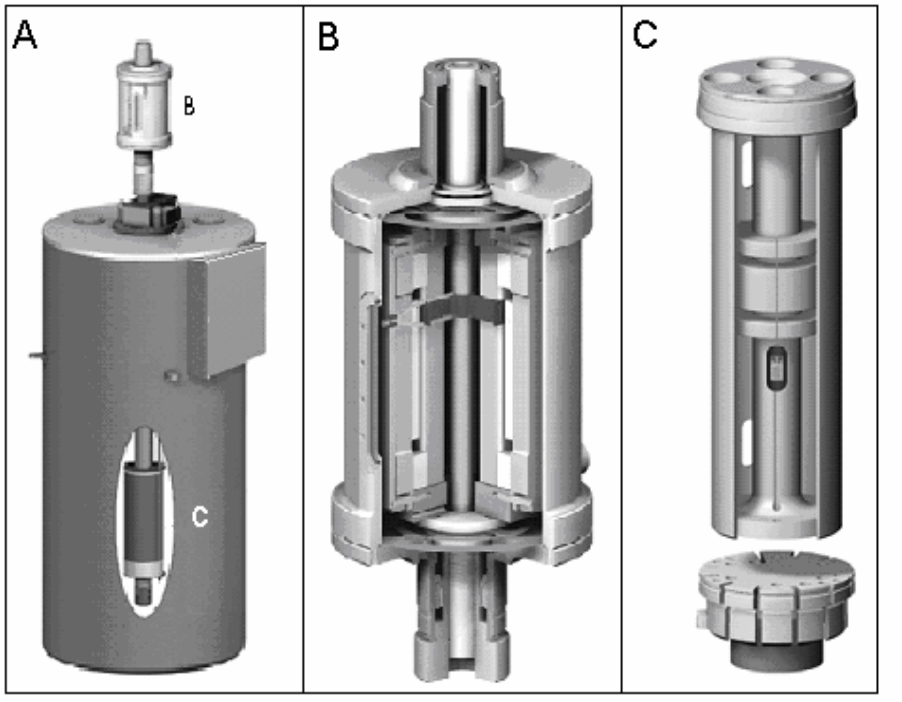


Figure 14: A) The VSM is situated atop to the PPMS from Quantum Design. B) The VSM head containing the linear drive motor. C) The induction coil set.

Millimeter-sized samples are carefully glued into copper sample holders using GE 7031 varnish. The sample holder is attached to a carbon fiber rod and inserted into the top of the VSM. M v. H plots were run at various temperatures.

RUS Setup and Experimentation

The RUS probe used in the experiment was custom fit for the PPMS system. The RUS design requirements roughly follow those described in a paper written by Migliori in 1996. The primary issue is that RUS systems must scan frequencies without affecting them. This requires a weak coupling between the sample and RUS transducers. In fact, the sample is only held in place by the weight of the top transducer. This weak coupling requires the electronics system to distinguish the signal from the noise. The RUS probe is shown below in Figure 15.



Figure 15: Our custom designed RUS probe option. Samples are situated between the two silver transducers in the left image.

Another key part to the design of an RUS system is the transducer. Transducers must not produce resonances in the range of interest. One workaround is to shift the transducer resonances to higher frequencies. This can be done by designing small and stiff transducers. Our system uses two transducers made out of $LiNbO_3$. Magnetic transducers have also been used in some setups but piezoelectric transducers are preferred. Magnetic transducers exhibit additional resonances in the drive coil and the drive coil's field may interact with the sample skewing RUS results (Migliori 1993).

Our electronics are shown in Figure 16. Our system is able to be compared to the typical RUS system shown in Figure 17. The electronics in our system are simplified but all the same elements remain. We also include a pre-amplifier to boost the RUS signal. The waveform generator replaces both the synthesizer and local oscillator. The mixer, filter, and A/D converter are a part of our SRB44 RF Lock-in Amplifier, which communicates to a computer running Labview software via GPIB.

Data collection is rather straightforward. A prepared sample is sandwiched between the transducers and the probe is carefully lowered into the PPMS. The PPMS is purged and sealed. A Labview RUS program is then modified to the user's defined frequencies and temperatures. The program is run, automating the PPMS and collection of data in field-cooled conditions. Depending on temperatures and frequencies, the program takes about a day to run. Ultrasound spectrum data take much longer to analyze.

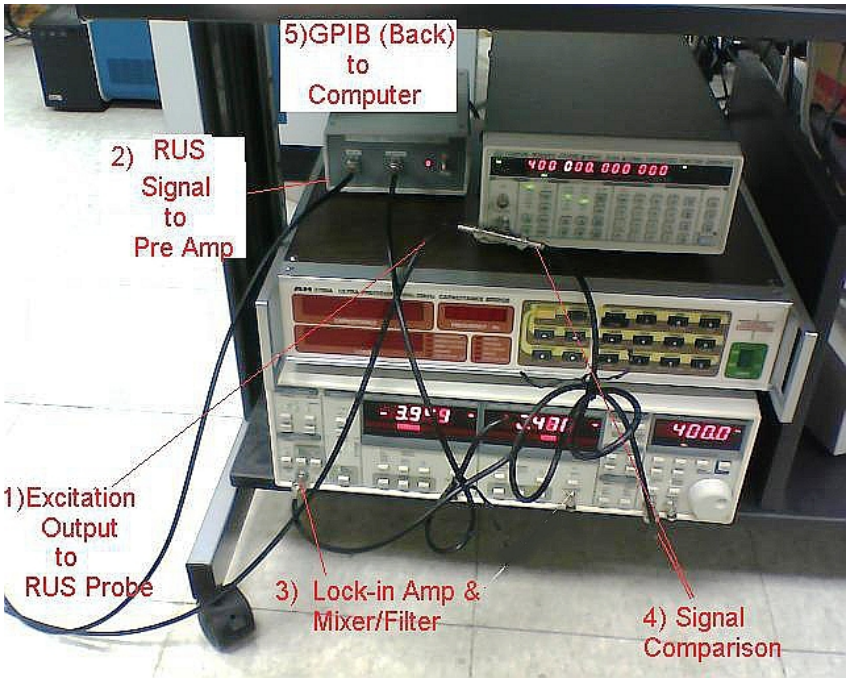


Figure 16: RUS electronics of the system used by our research group.

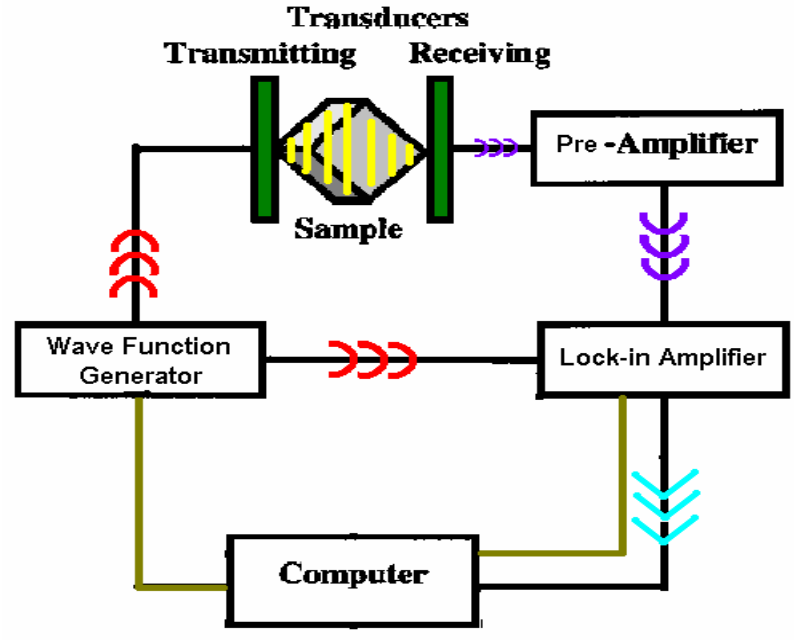


Figure 17: The typical RUS setup.

Finally, the data consists of in-phase and out-of-phase quadrature components. These components are plotted up as a spectrum which can be phase shifted to find maxima corresponding to the attenuation of a resonance. These peak positions are recorded and imported into Microsoft Excel then organized by hand. Human errors are generally caught at this step. Next, the frequencies at each temperature are inserted into the RPR code from Albert Migliori and William Visscher producing a single fit of the resonant frequencies. Numbers from each fit are extracted to form plots of the elastic moduli.

CHAPTER IV

RESULTS AND DISCUSSION

Polycrystalline samples that are isotropic have two independent moduli: the c44 modulus which corresponds to the shear modulus, and the c11 modulus which corresponds to a longitudinal modulus. These moduli have physical significances to sound velocities and define the Young's modulus, bulk modulus, and Poisson's ratio (Schreiber 1973).

$$G = C_{44} \quad \textbf{and} \quad E = 3C_{44} - \frac{{C_{44}}^2}{(C_{11} - C_{44})}, \quad \textbf{(53)}$$

$$\nu = \frac{1}{2} - \frac{C_{44}}{2(C_{11} - C_{44})} \quad \textbf{and} \quad B = C_{11} - \frac{4}{3}C_{44} \quad \textbf{(54)}$$

We used RUS as a function of temperature and magnetic field to determine the elastic moduli of Tb_6FeSb_2 and Tb_6FeSb_2. No appreciable hysteresis was found upon heating or cooling within RUS. The C_{11} for Tb_6FeBi_2 is shown in Figure 18; C_{44} modulus is shown in Figure 19. RPR code fits were ran on all the temperatures to calculate moduli. An example of an input file for RPR is found in the Appendix for Tb_6FeBi_2, along with a few RPR output files. Hundreds of fits were completed for almost every temperature to establish a baseline in the data. This baseline was used in conjunction with individual resonant frequencies to display the moduli. For Tb_6FeBi_2, goodness of fit values started at 0.32% and remained below 0.4% with only a couple missing modes. These modes were weighted zero to ensure the fit. This indicates the results are acceptable. Absolute errors were 1% for C_{11} and under 1% for C_{44}.

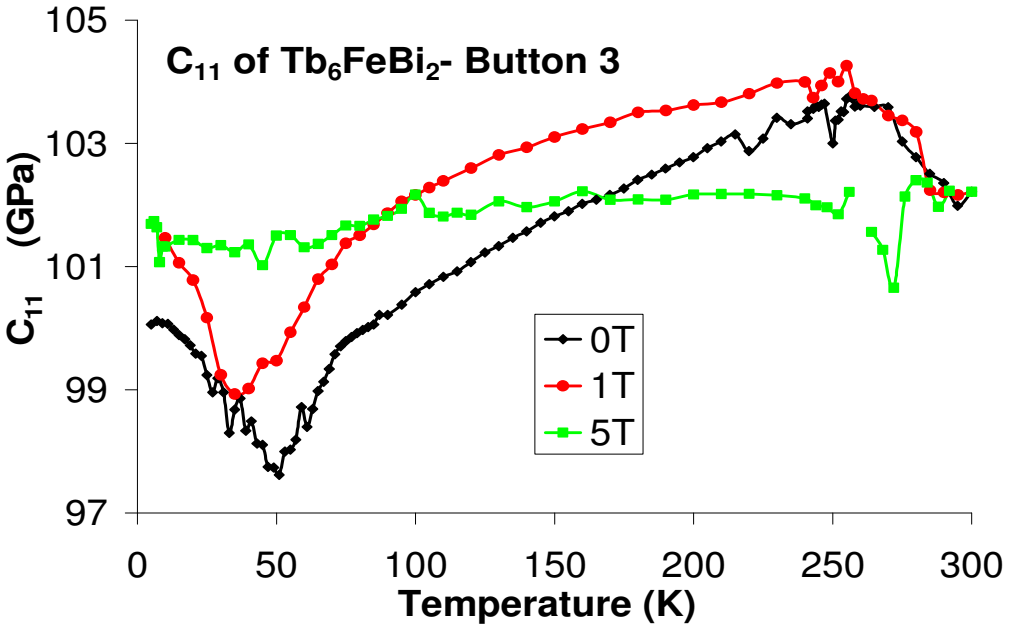


Figure 18: C_{11} of Tb_6FeBi_2 as a function of field and temperature. Error within 1%

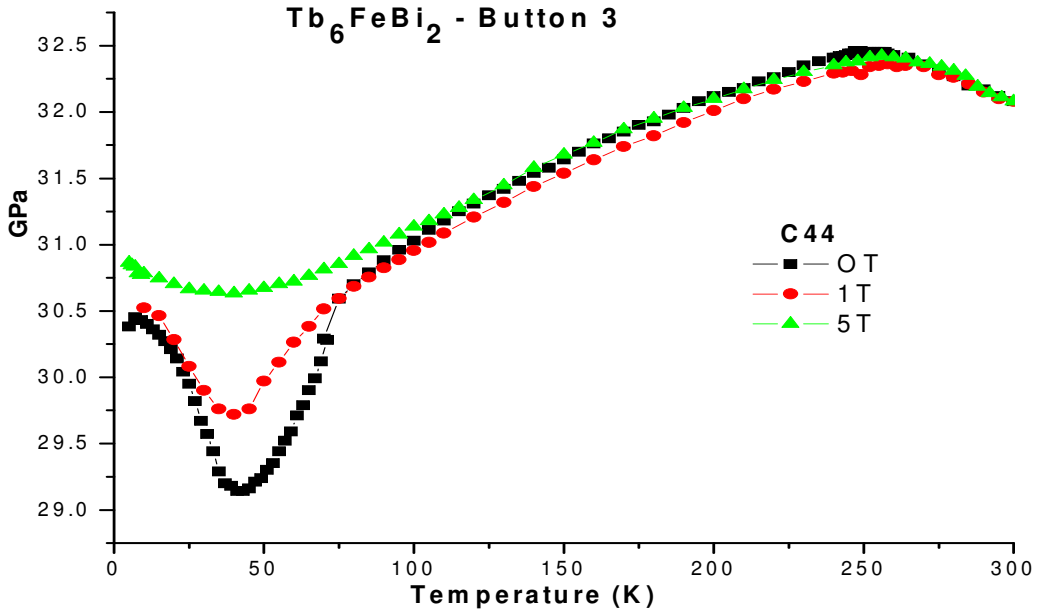


Figure 19: C_{44} modulus of Tb_6FeBi_2 as a function of field and temperature.

Starting from room temperature upon cooling, RUS notices a change in the first derivative of the elasticity. This change is observed at T=250K, which we know to be the Curie temperature (Tc) for this compound from literature (He 2007). Curie transitions affect some modes more than others so it is important to look at both moduli. Upon application of a magnetic field, the C_{11} modulus shows a flattening when spontaneous magnetization sets in. This is to be expected but C_{11}'s data can only be taken as qualitative since the errors are high. C_{44} does not show much effect with field in the vicinity of Tc, implying that the Curie transition is not affected greatly by magnetic fields.

Next, the positive derivative of C_{44} below the Curie temperature is an indication of approaching a structural phase transition at low temperatures. Most materials generally increase in hardness with decreasing temperature. This major softening of the moduli below 250K therefore suggests that a structural transition occurs near 50K. However, no structural transition has been reported for this material. Furthermore, XRD data at 11K for Tb_6FeSb_2, with similar trends, show it remains hexagonal. This softening may be related instead to a magnetic transition. Magnetic fields also seem to suppress this low temperature transition. Neutron diffraction experiments are scheduled this summer to shed light on this transition.

Other dependant moduli and important values can be calculated from C_{44} and C_{11}. Young's modulus ratio is given in Figure 20. Poisson's Ratio is also calculated as a function of temperature and shown in Figure 21. The value for Tb_6FeBi_2's Poisson's ratio is average for a metal. These moduli are consistent with prior analysis of C_{44} and C_{11}. Data for Tb_6FeBi_2's bulk modulus, which relies heavily upon C_{11}, appear inconclusive.

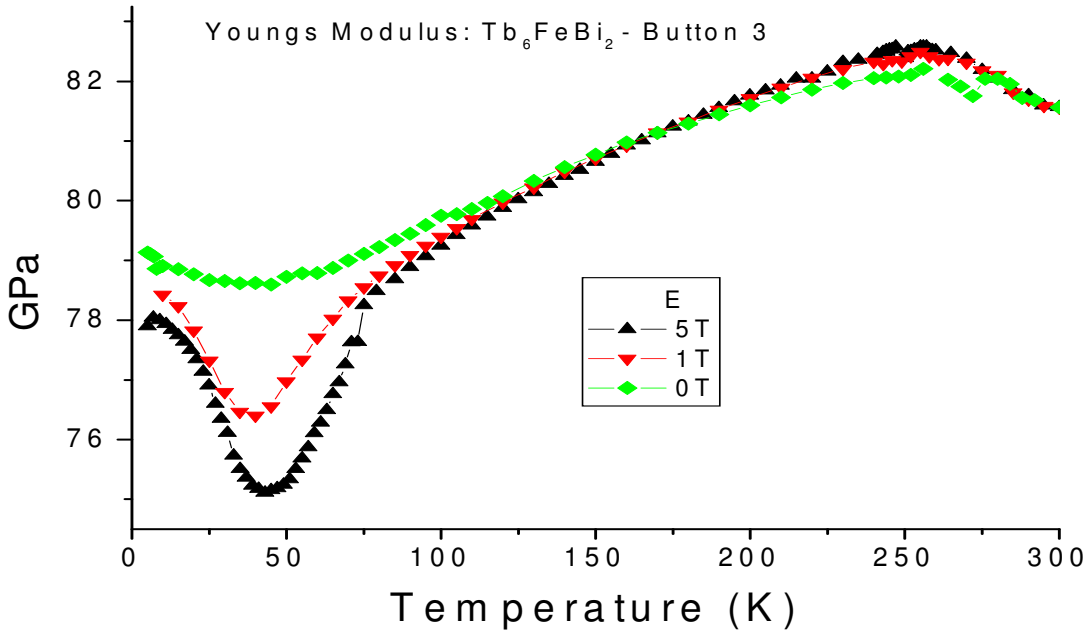


Figure 20: Young's Modulus of Tb_6FeBi_2 as a function of field and temperature.

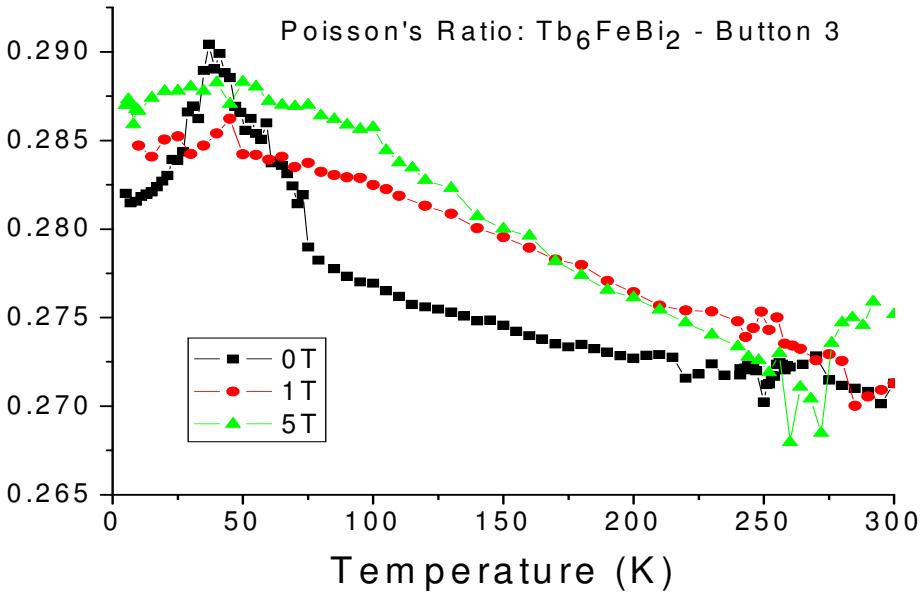


Figure 21: Poisson's ratio of Tb_6FeBi_2 as a function of temperature and field.

Tb_6FeSb_2 was examined by RUS under magnetic fields between 0 and 9T. Tb_6FeSb_2 behaves very similar to Tb_6FeBi_2. There are some differences to note between the compounds and the data collected. The Tb_6FeSb_2 sample was of much higher quality than Tb_6FeBi_2's sample. This improved sample quality allows for better resolution and insight into the two transitions. Another Tb_6FeSb_2 RUS sample was created by a different synthesis batch to confirm the results presented below. The temperatures at which the various magnetic transitions occur are slightly higher in Tb_6FeSb_2 when compared to Tb_6FeBi_2. Tb_6FeSb_2 shows greater variability in low fields. The C_{44} modulus is shown in Figure 22 and again near the Curie temperature in Figure 23.

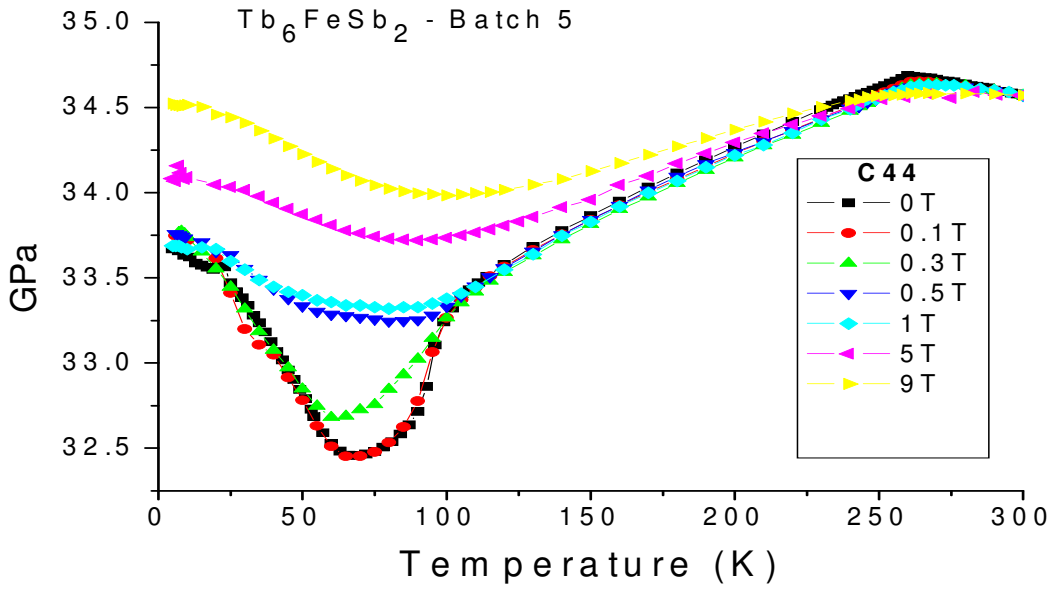


Figure 22: C_{44} of Tb_6FeSb_2 as a function of field and temperature.

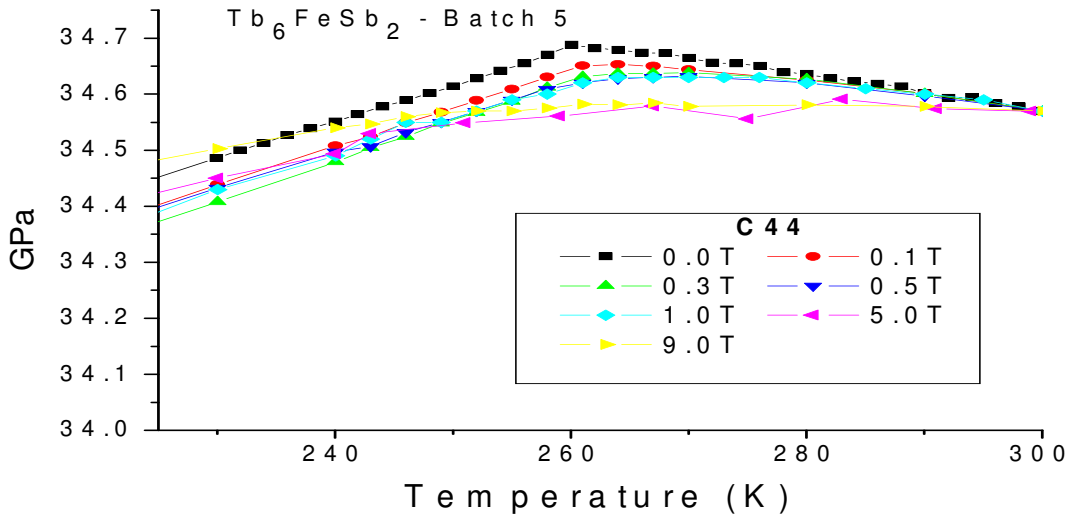


Figure 23: C_{44} of Tb_6FeSb_2 near the Curie temperature.

The similarities between Tb_6FeBi_2 and Tb_6FeSb_2 indicate that the lattice is not largely affected by the bismuth vs. antimony substitution. The similarity in magnetic properties implies that terbium atoms do not exhibit much interaction via adjacent neighbors. Most of the differences in magnetism can probably be related to the slightly smaller lattice of Tb_6FeSb_2. The lattice constants of our Tb_6FeSb_2 samples are a=4.180Å and c=8.182Å, while Tb_6FeBi_2's constants are a=4.201Å and c=8.287Å.

We also observe that C_{44} flattens out near the Curie temperature in magnetic fields. The Curie temperature also shifts to slightly higher temperatures when stronger fields are applied. This is consistent with field stabilized magnetization. This size of this temperature shift in part depends upon the energies required to form domains. The shift of the Curie temperature is relatively small in Tb_6FeSb_2.

C_{11} is shown in Figure 24 and in Figure 25.

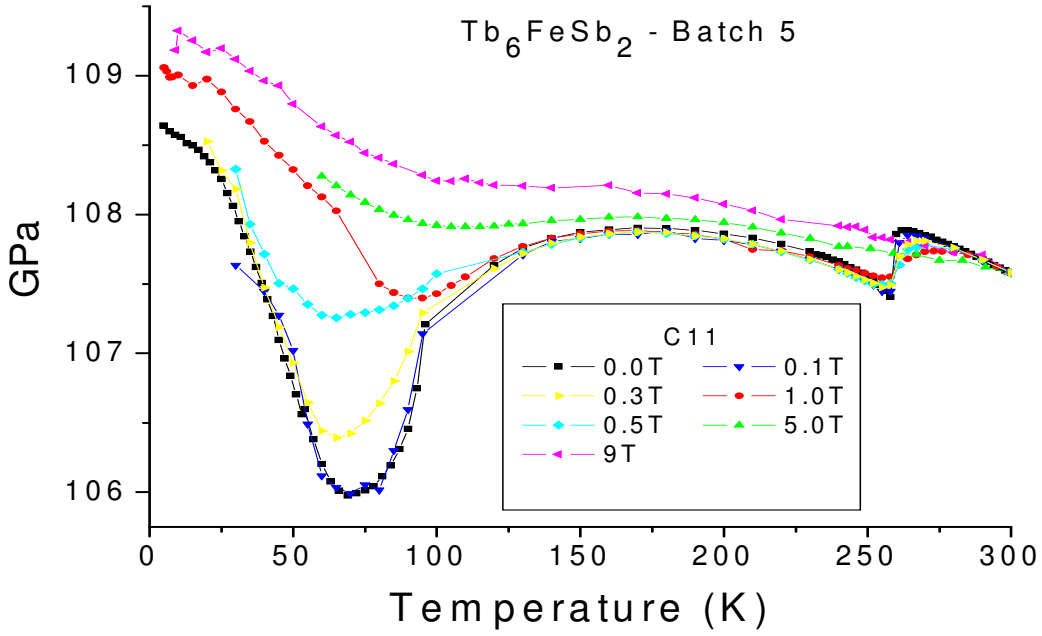


Figure 24: C_{11} of Tb6FeSb$_2$ as a function of field and temperature.

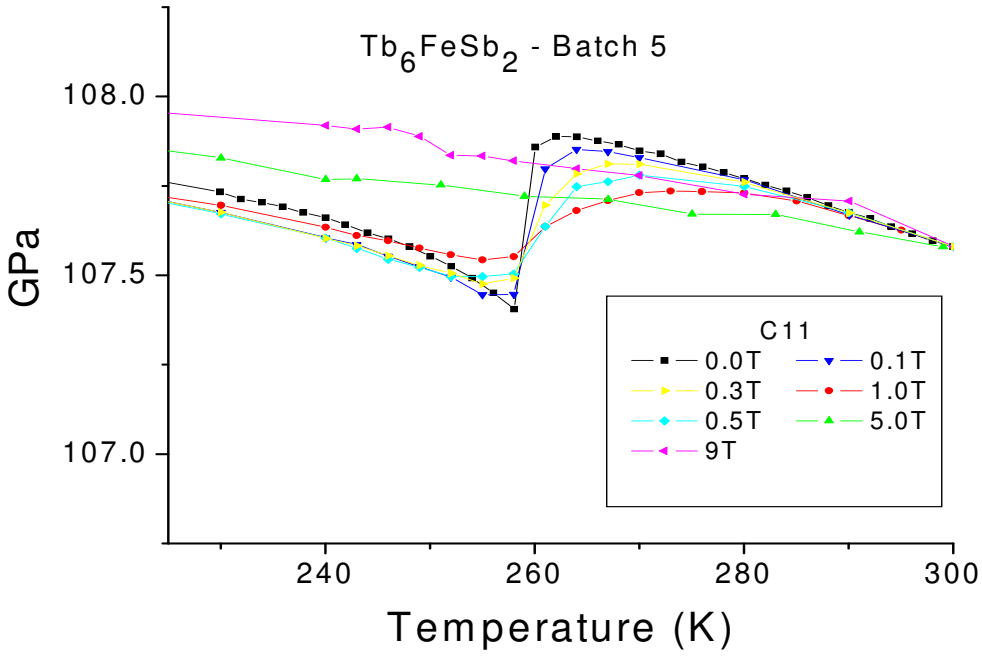


Figure 25: C_{11} of Tb6FeSb$_2$ near the Curie temperature.

The discontinuity of C_{11} in zero field shows that C_{11} is more affected by the magnetic transition than C_{44}. C_{11} also shows the suppression of the spontaneous magnetization transition in higher fields. This indicates that the magnetization reached its saturation above 260K and the Curie temperature is ill-defined. RUS data indicate that the maximum magnetic saturation of Tb_6FeSb_2 occurs between 1T-5T. C_{11} shows a similar response as C_{44} near the lower temperature magnetic transition. The percent that C_{11} rebounds is higher than C_{44} and it is unusual that this modulus rebounds to a higher value upon cooling through the transition. C_{11}'s and C_{44}'s linear increase, followed by tapering off, at very low temperatures is the standard behavior of most materials. From C_{44} and C_{11} the Young's modulus and Poisson's ratio can be calculated. These are shown in Figure 26 and Figure 27. The Poisson's ratio for Tb_6FeSb_2 is a little smaller than the one found for Tb_6FeBi_2.

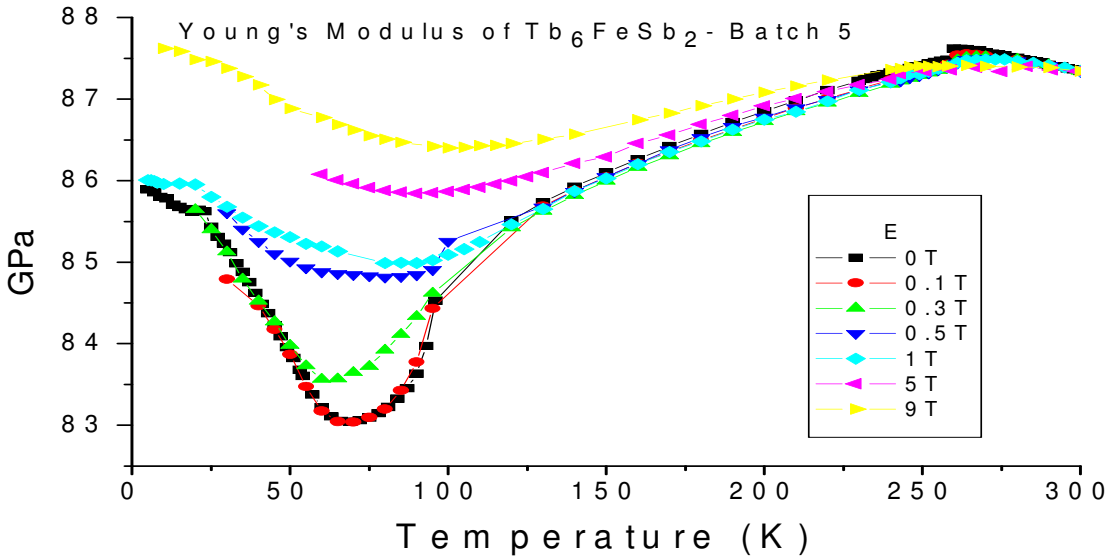


Figure 26: The Young's modulus of Tb_6FeSb_2 as a function of field and temperature.

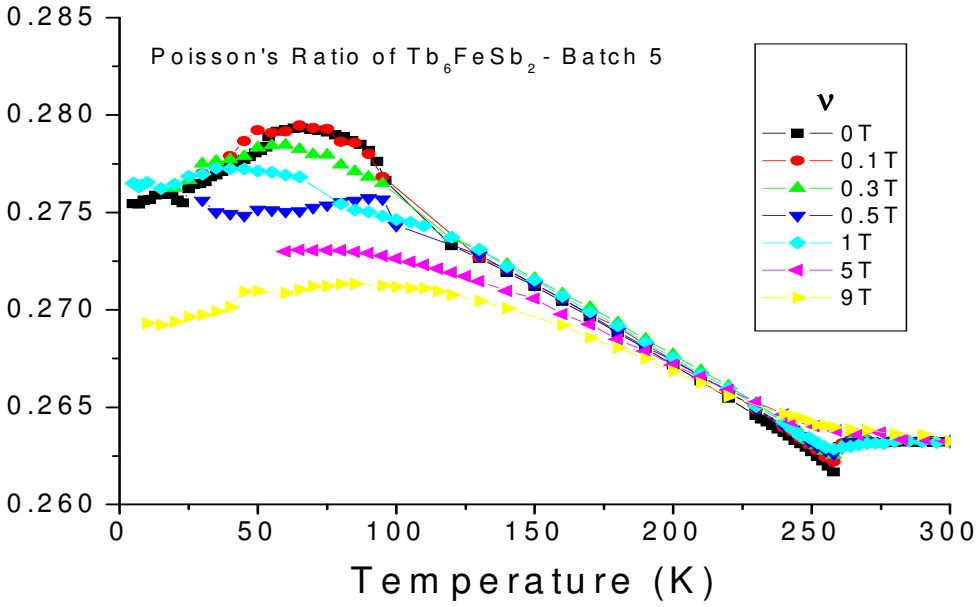


Figure 27: Poisson's ratio for Tb_6FeSb_2 as a function of temperature and field.

High magnetic fields suppress and shift Tb_6FeSb_2's low temperature magnetic transition. The low temperature transition range is 55-95 K in the Tb_6FeSb_2. When compared to Tb_6FeBi_2 in field, Tb_6FeSb_2 transition moves to higher temperatures (up to 120K) instead of to lower temperatures as in Tb_6FeBi_2. Finally, we must consider that a 9 Tesla magnetic field, which is the maximum our system can produce, is still causing effects in the material. These large fields are somehow contributing to a change in the material's low temperature magnetic transition in tangible ways. This is even after large fields have already saturated the magnetic moments in these compounds. RUS has provided many answers but left us with many questions.

Structural Involvement

Our group doped Tb_6FeX_2 with Co into the Fe site providing additional information about the low temperature transition. C_{44} of various Co-doping levels are displayed in Figure 28 and Figure 29. This doping produced softening of 15-20% with temperature in C_{44} vs. 4% softening in the parent compounds. Large changes in the elasticity measured by RUS indicate a structural transition. XRD data at low temperatures confirmed a structural change in $Tb_6Fe_{(1-x)}Co_xSb_2$. Thus, the proposed non-collinear ferromagnetic transition in literature may be something that is weakly coupled to a structural transition normally suppressed in the parent compound. Neutron scattering data is planned to shed light on this transition. We realize it is too early to say much about this new structure. The data is undergoing Rietveld refinement.

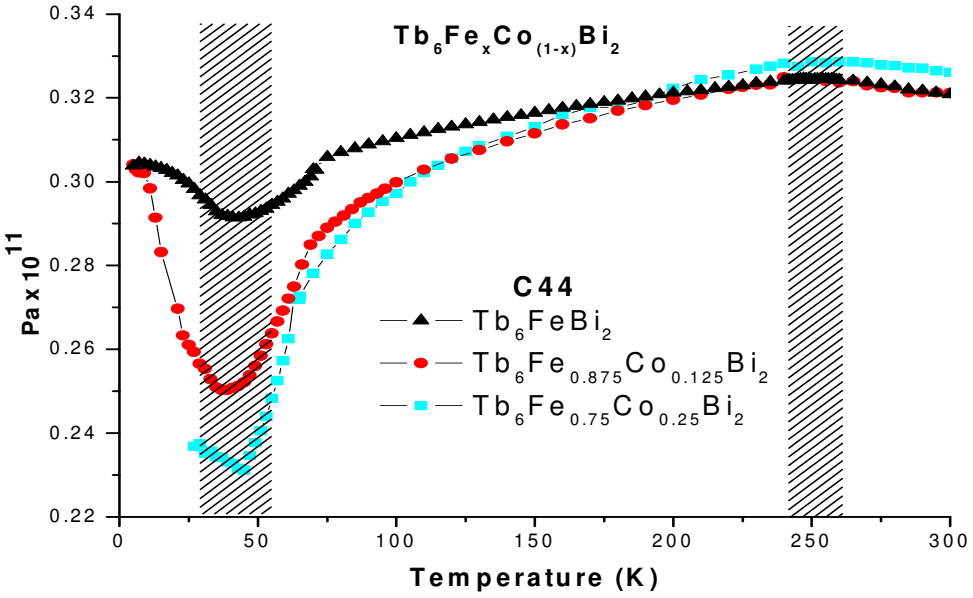


Figure 28: Effects of Cobalt substitution on Tb_6FeBi_2 suggest structural changes.

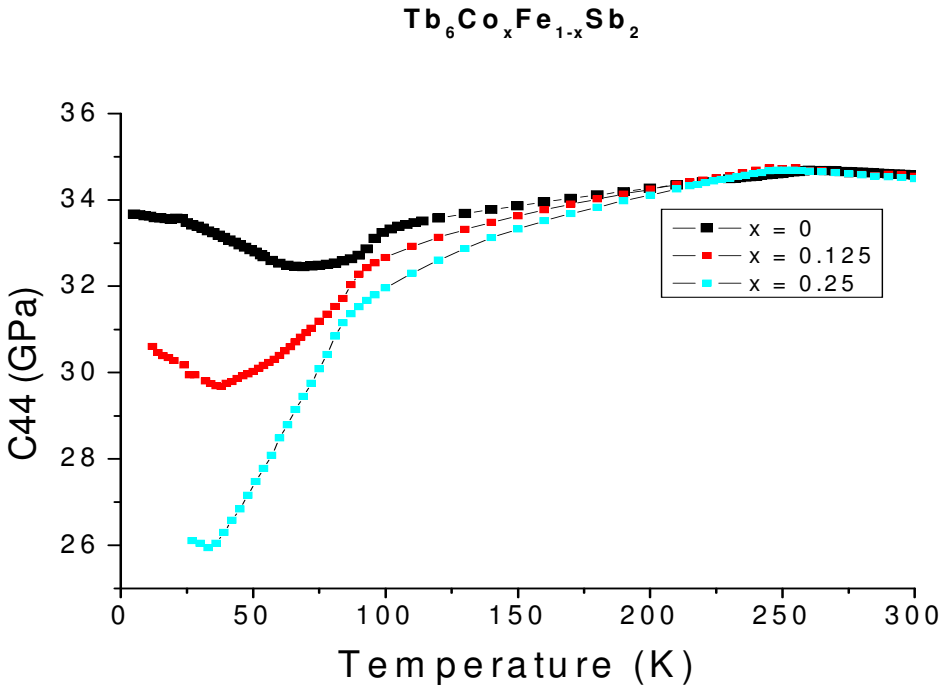


Figure 29: Effects of Cobalt substitution on Tb_6FeSb_2 also suggest structural changes.

There is plenty of RUS data still being gathered on the co-doped Tb_6FeSb_2 series. These RUS findings indicate there is still much to be known about these new alloys.

Magnetization

Using the VSM option, magnetization data was taken for the various samples down to 50K. We also collected a series of magnetization (M vs. H) data at various temperatures. Tb_6FeSb_2 high temperature data in Figure 30 show the soft behavior as reported by He's group in 2007. We also report this behavior for the first time in Tb_6FeBi_2 in Figure 31. Quantitatively, Tb_6FeBi_2 shows a little less magnetism than Tb_6FeSb_2 consistent with previous papers.

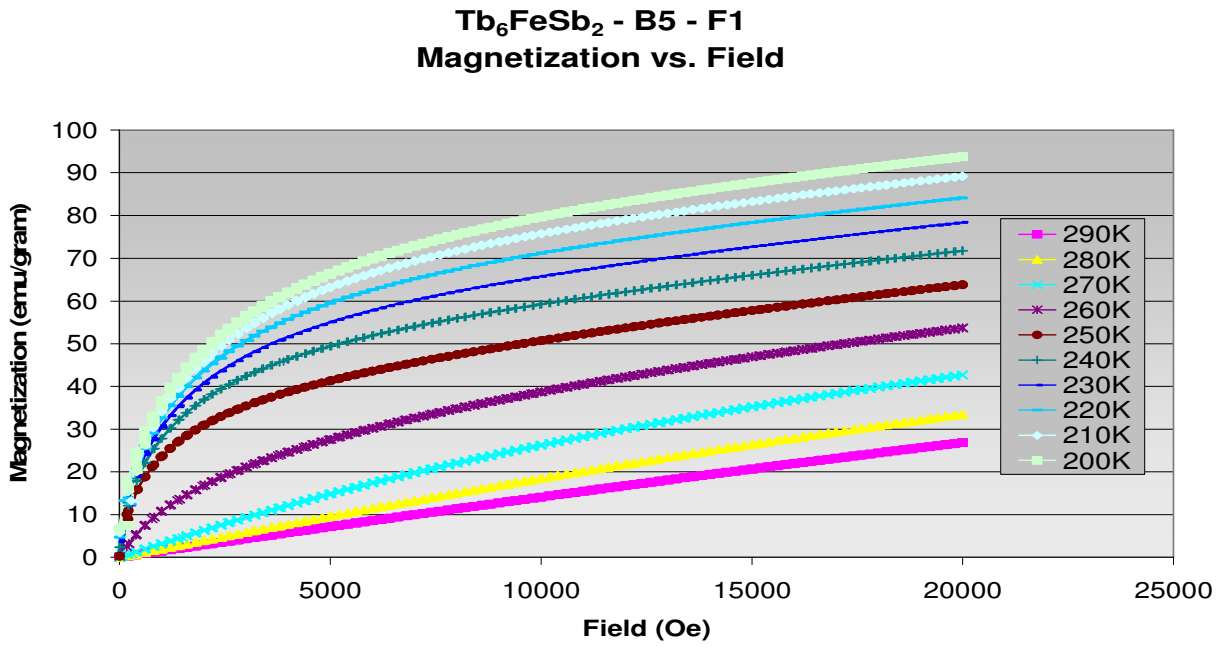


Figure 30: High temperature M v. H data for Tb_6FeSb_2.

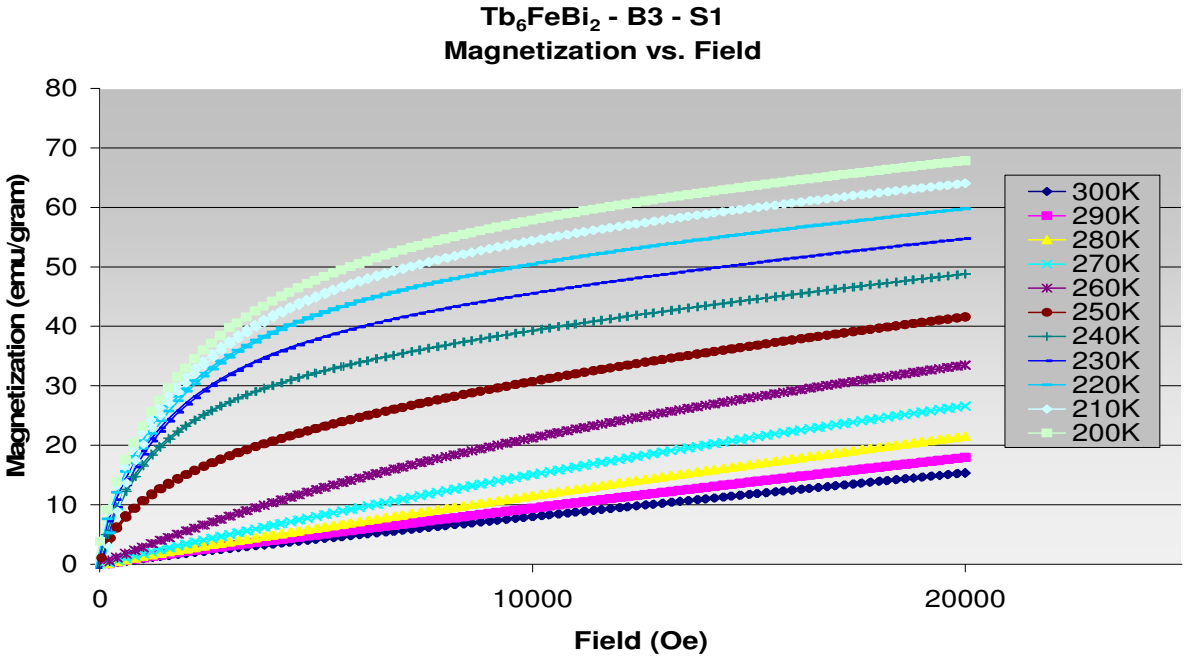


Figure 31: High temperature M v. H data for Tb_6FeBi_2

Furthermore, this magnetization data fit with a hexagonal structure, in which full saturation of magnetization is rarely reached. The easy axis strongly favors c-axis of the hexagonal structure.

Magnetization (M v. H) data was taken between 50-130K for Tb_6FeSb_2 and Tb_6FeBi_2. These low temperatures show magnetic hysteresis in Tb_6FeBi_2 and Tb_6FeSb_2. This data is shown in Figure 32 and Figure 33. These measurements examine if the magnetic behavior at these temperatures may be linked to the low temperature transition in these materials. The hysteresis loops show increasing coercivity, magnetization, and remanence at low temperatures, approaching the transition.

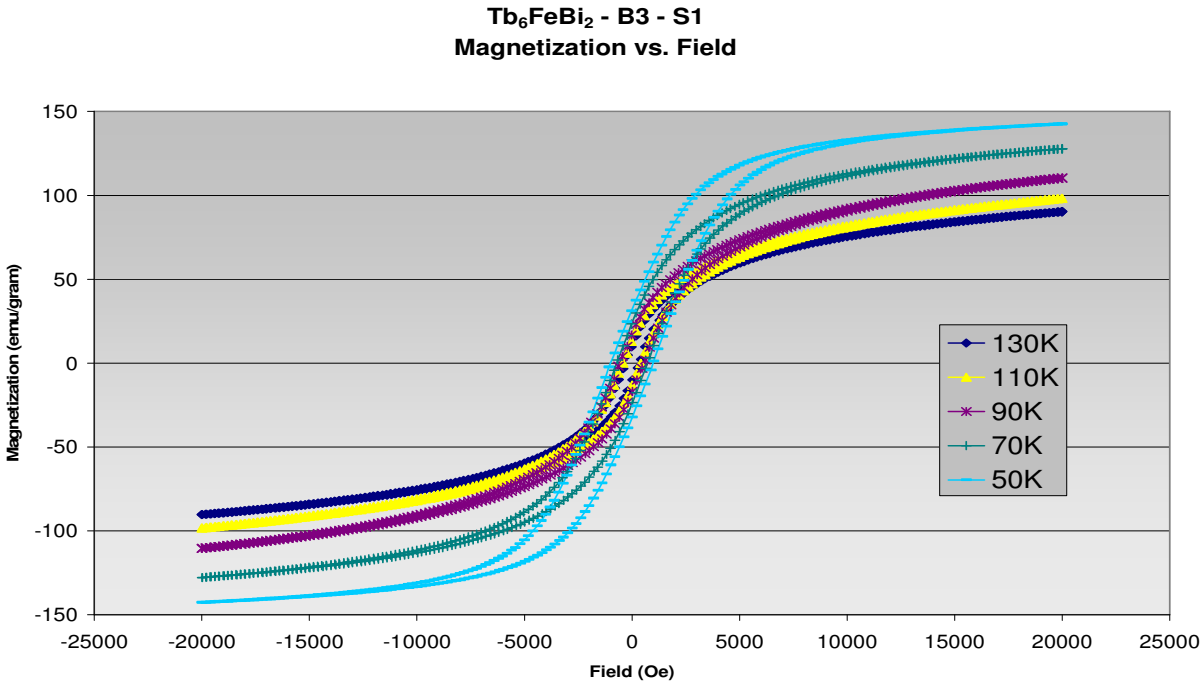


Figure 32: Magnetization data of Tb_6FeBi_2 between 50-130K.

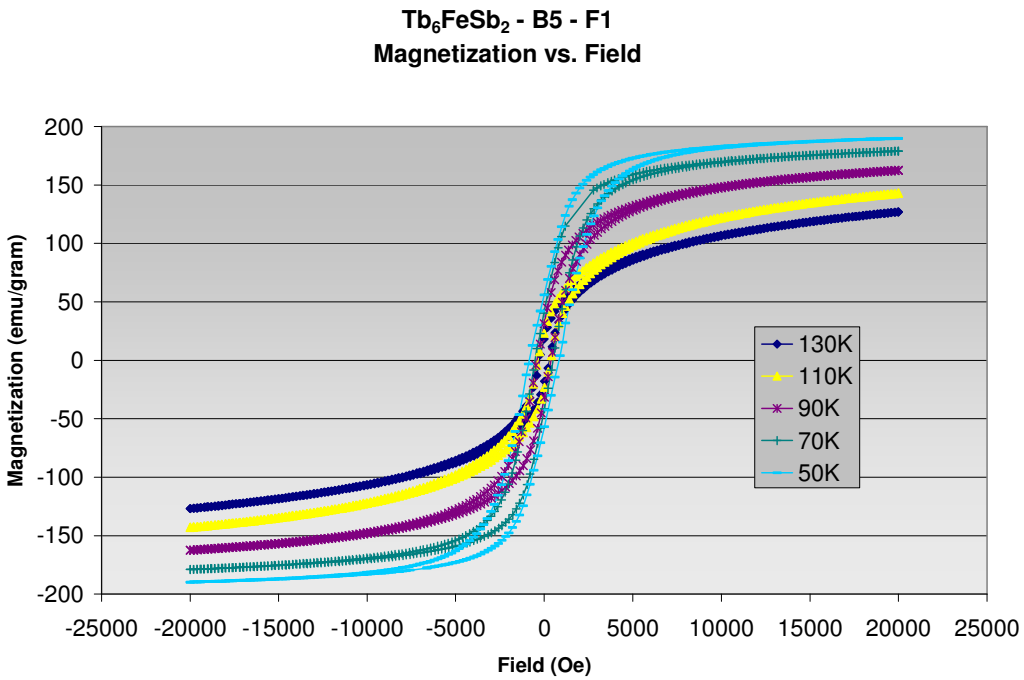


Figure 33: Magnetization data of Tb_6FeSb_2 between 50-130K.

The change in hysteresis loop is indications additional energy expended in magnetization. This energy change of magnetization may arise from: magnetocrystalline anisotropy, magnetostriction, or some other time-temperature dependent causes. The measured coercive fields for Tb_6FeSb_2 and Tb_6FeBi_2 decrease linearly upon warming from 80K and 100K, as shown in Figure 34. This linear region corresponds to the magnetocrystalline anisotropy decreasing with increasing temperature (Spaldin 2003). The low temperature deviation from this linear trend in coercivity is the material dipping below a moment relaxation temperature. This is supported by Tb_6FeBi_2 exhibiting relaxation at higher temperature than Tb_6FeSb_2. It does not appear to be related to the transitions because Tb_6FeBi_2 has a lower transition temperature. This anomaly should follow the transition if they were related phenomena; instead we believe it is a temperature-time dependent effect.

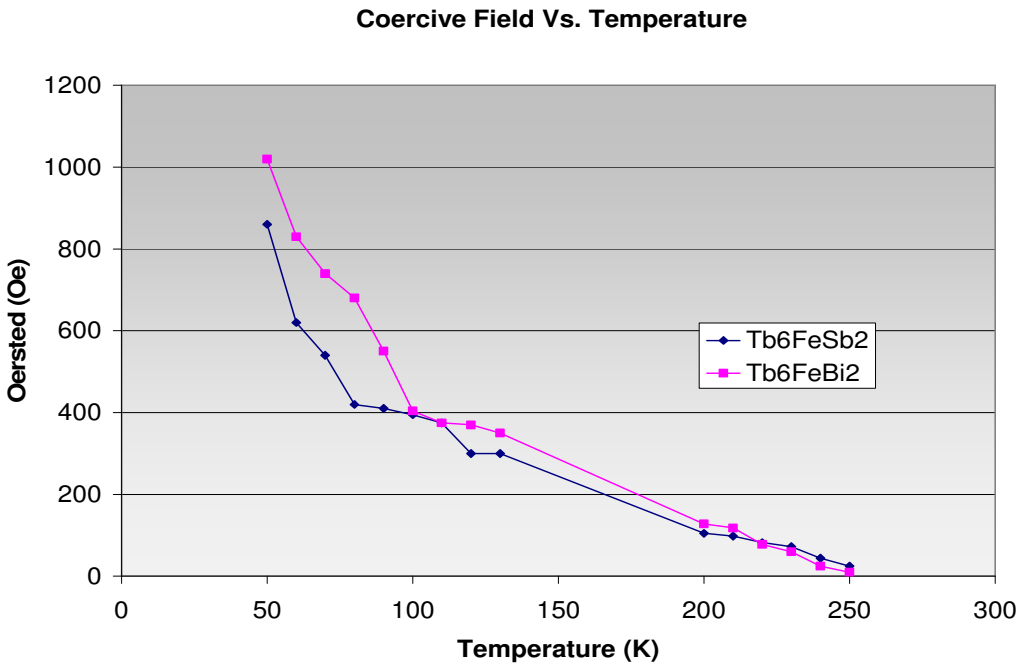


Figure 34: Coercive Fields vs. Temperature of Tb_6FeSb_2 and Tb_6FeBi_2.

CHAPTER V
FUTURE WORK AND CONCLUSIONS

We have used Resonant Ultrasound Spectroscopy to examine Tb_6FeSb_2 and Tb_6FeBi_2. RUS proved to be an excellent method in studying these new magnetic materials. RUS examined the Curie temperature near 250K with a good amount of detail. The C_{44} and C_{11} moduli each provide a different viewpoint to what is happening near the two transitions for Tb_6FeX_2. C_{44} shows a sharp change in the derivative of elasticity and C_{11} shows a discontinuous drop at the Curie temperature. At low temperatures, C_{11} and C_{44} both decrease at similar proportions.

The interpretation of RUS for the first transition is pretty straight forward. The spontaneous magnetization in field near the Curie temperature shows that the Curie temperature is not largely affected by the magnetic field. The Curie temperature becomes ill-defined in large magnetic field since paramagnetic saturation is reached prior to the spontaneous ordering to ferromagnetism. RUS data provided approximate values for the magnetic saturation of the two materials by their effect in suppressing the Curie transition. These saturation values were reproduced by VSM magnetization measurements. Large fields still have an effect on the sample but the effect is related to incomplete magnetization from the c-axis, as seen in RUS and M v. H.

RUS also provided a lot of insight into the low temperature transition that few other techniques could rival. Yet, this insight has left us with more questions. The lower temperature transition of Tb_6FeSb_2 and Tb_6FeBi_2, which was previously reported as a collinear ferromagnetic to non-collinear transition, appears more complex than just that. The softening below the Curie temperature of the $Tb_6Co_xFe_{(1-x)}Sb_2$ and $Tb_6Co_xFe_{(1-x)}Bi_2$

series suggests that structural transition of parent compounds is imminent. The low temperature x-ray diffraction data suggest that this transition never occurs for the parents. This lets us postulate the effect is from a change in the magneto-elastic coupling.

The questions raised by RUS, about the low temperature transition, will lead us to future work to explain RUS's findings in more meaningful ways. This work will include neutron scattering experiments to probe the magnetic structures of these materials. Neutron scattering will simultaneously provide accurate information on the crystal structure, as well as change that it undergoes. We desire to also determine how the structural transition is coupled to magnetism in the Co-substituted series. The examination of the structural transition will help us determine the source of the magnetic transition. In addition, conducting an inelastic neutron scattering study will determine the nature of the elastic softening as seen in RUS.

One important part of this project still remains in our future work, magnetostriction. Unfortunately, our initial attempts to measure magnetostriction have turned up mixed results. We are still calibrating our equipment with standard materials. The measurement requires a high resolution capacitance bridge, which measures the spacing between two capacitance plates in a fully compensated dilatometer. The dilatometer will easily produce thermal expansion values for the material as well. Magnetostriction primarily arises from elasticity and the spin-orbit coupling. Initial measurements of magnetostriction for Tb_6FeBi_2 suggest that magnetostriction is negative on the order of 100-200 microstrain with the maximum magnetostriction at the low temperature transition. This value for magnetostriction is about average for a rare-

earth magnetic compound. Yet, more measurements will need to be taken for confirm this value. More measurements will need to be taken for Tb_6FeSb_2 and Co-substituted compounds. These compounds may show different values for magnetostriction.

We plan on synthesizing more Zr_6CoAs_2 type compounds with other rare earths. Morozkin's paper in 2004 is sufficient to show that this family of compounds is not fully explored and has a lot of diversity. His papers show that different magnetic behaviors exist for a wide range of rare earths and dopants. We plan to substitute other transition metals like manganese into the Tb_6FeSb_2 lattice. We hope to find a compound with near room temperature curie temperature. We expect to find some similarities to Tb_6FeX_2. Magnetization vs. temperature and magnetostrictive measurements will come out for these compounds as soon as they are fully reproducible.

This research has furthered our basic understanding of elasticity and magnetism. RUS has been useful in uncovering the link between magnetism and elasticity. This link is shown to consistently produce interpretable results in RUS. These results show a strongly coupling with the magnetic structure of the material.

Tb_6FeX_2 with X= Sb,Bi may not have fit our desired properties. Sample preparation experience shows that this material is brittle. The magnetostriction is not as high as we were originally hoping for. Yet, Tb_6FeX_2 is a new material that hasn't been studied before. The elasticity and magnetism of this system has however given us some experience of what to expect for future compositions and compounds in our search for new magnetostrictive materials.

REFERENCES

LIST OF REFERENCES

Abbundi, R. and A. E. Clark. “Anomalous Thermal Expansions and Magnetostriction of Single Crystal Tb.27Dy.73Fe2” IEEE Transactions on Magnetics, MAG-13, 1519-1520. 1977

Cai, Gemei; Jiliang Zhang et al. “Crystal structure and Magnetic properties of Tb_6FeSb_2“ Journal of Alloys of Compounds. Vol 421. 42-44. 2006.

He, Wei; Jiliang Zhang et al. “Thermomagnetic Properties Near Transitions of Tb_6FeX_2 (X=Sb, Bi)” Journal of Alloys and Compounds. Vol 443. 15-19. 2007.

Leisure, R.G. and F. A. Willis. “Review: Resonant Ultrasound Spectroscopy.” J. Phys. Condens. Matter 9. pg 6001-6029.1997.

Maynard, Julien. “Resonant Ultrasound Spectroscopy”. Physics Today. January. pg 26-31. 1996.

Migliori, Albert and Timothy W. Darling. “Resonant Ultrasound Spectroscopy for Materials Studies and non-destructive Testing.” Ultrasonics. Vol 34. pg 473-476. 1996.

Migliori, Albert and John L. Sarrao. Resonant Ultrasound Spectroscopy: applications to physics, materials measurements, and nondestructive evaluation. Wiley-interescience publication. 1997.

Migliori, Albert and J. D. Maynard. “Implementation of Modern Resonant Ultrasound Spectroscopy System for the Measurement of Elastic Moduli of Small Solid Specimens” Review of Scientific Instruments. Vol. 76, Article 121301. 2005.

Migliori, A.; J. L. Sarrao; et al. “Resounant Ultrasound Spectroscopic Techniques for Measurement of Elastic Moduli of Solids”. Physica B. Vol 183. pg 1-24. 1993.

Morozkin, A. V.; V.N Nikiforov and B. Malaman. “Magnetic Structure of the Zr_6CoAs_2 – type Tb_6FeBi_2 compounds” Journal of Alloys and Compounds. Vol 393. pg L6-L9. 2005.

Morozkin, A. V. “Magnetic Structure of the Zr_6CoAs_2 –type Ho_6FeSb_2, Ho_6FeBi_2 and Ho_6MnBi_2 compounds” Journal of Alloys and Compounds. Vol 395. pg 7-16. 2005.

Pantea, Christian, Dwight G. Rickel et al. "Digital Ultrasound Pulse-echo Overlap System and Algorithem for Unambiguous Determination of Pulse Transit Time." Review of Scientific Instruments. Vol 76. Art. 114902. 2005.

Schreiber, Edward et al. Elastic Constants and Their Measurement. McGraw-Hill. 1973.

Schwarz, R.B. and J. F. Vuorinen. “Resonant Ultrasound Spectroscopy: Applications, Current status, and Limitations. “ Journal of Alloys and Compounds. Vol. 310. pg 243-250. 2000.

Spaldin, Nicola. Magnetic Materials: Fundamentals and Device Applications. Cambridge University Press. 2003.

SWT Physics Department “Vibrating Sample Magnetometer” Texas State University. 22 May 2006. Web. 8 April 2010. <http://uweb.txstate.edu/~ab35/manuals/VSM/vsm.pdf>

“Vibrating Sample Magnetometer” Quantum Design USA. September 2005. Web. 8 April 2010. <http://www.qdusa.com/products/brochures/vsmappnote9-05.pdf>

APPENDIX

Table 3: The bond lengths and number of nearest neighbors of each atom in Tb_6FeSb_2

Atomic	BL (Å)	d(Å)	δ(%)	CN
Fe				
6Tb1	2.846	3.023	5.855	9
3Tb2	3.296	3.023	-9.031	
Sb				
3Tb1	3.206	3.221	0.466	9
6Tb2	3.255	3.221	-1.056	
2Fe	2.846	3.023	5.5855	
2Sb	3.209	3.221	0.466	
Tb1				
2Tb1	3.349	3.564	6.033	12
4Tb2	3.548	3.564	0.449	
2Tb2	3.636	3.564m	-1.740	
1Fe	3.296	3.023	-9.031	
Tb2				
4Sb	3.255	3.211	-1.056	11
2Tb1	3.626	3.564	-1.740	
4Tb1	3.548	3.564	0.449	

An example of RPR Code input file called “RUSin”

…

```
Tb6FeBi2 - Batch 3 - .064 gm - 300K
2 0 10 0  0.064  1.00 1 0 0 0 0 0 0 0 0 0
.97  0.3
0.1593  0.16441  0.25696
0.33246473   0.33246473          0
0.40557857   0.40557857          1
0.41098048   0.41098048          1
0.54918436   0.54918436          1
0.56395599   0.56395599          1
0.57061811   0.57061811          1
0.58067289   0.58067289          1
0.64513864   0.64513864          1
0.66243234   0.66243234          1
0.71091482   0.71091482          1
0.72323339   0.72323339          1
0.73521465   0.73521465          1
0.74380986   0.74380986          1
0.76473751   0.76473751          1
0.7815074    0.7815074           1
0.80475557   0.80475557          1
0.80475557   0.80475557          1
0.85123828   0.85123828          1
0.85277198   0.85277198          1
0.85776129   0.85776129          1
0.86690448   0.86690448          1
0.86861838   0.86861838          1
0.86992674   0.86992674          1
0.88522006   0.88522006          1
0.89189142   0.89189142          1
0.90953737   0.90953737          1
0.91629504   0.91629504          1
0.91959205   0.91959205          1
0.92785745   0.92785745          1
0.9593095    0.9593095           1
0.96941717   0.96941717          1
0.98006102   0.98006102          1
0.99295413   0.99295413          1
```

…

This produces the following output for $Tb_6.FeBi_2$ in zero field.

…

Tb6FeBi2 - Batch 3 - .064 gm - 300K
free moduli are c11, c44
using 10 order polynomials mass= 0.0640 gm rho= 9.510 gm/cc

n	fex	fr	%err	wt	k	i	df/d(moduli)	
1	0.332465	0.327093	-1.62	0.00	4	1	0.00	1.00
2	0.405579	0.404877	-0.17	1.00	1	2	0.19	0.81
3	0.410980	0.409845	-0.28	1.00	7	2	0.19	0.81
4	0.549184	0.551644	0.45	1.00	5	1	0.13	0.87
5	0.563956	0.563900	-0.01	1.00	8	2	0.04	0.96
6	0.570618	0.572653	0.36	1.00	2	2	0.04	0.96
7	0.580673	0.576121	-0.78	1.00	4	2	0.00	1.00
8	0.645139	0.643395	-0.27	1.00	3	2	0.04	0.96
9	0.662432	0.659196	-0.49	1.00	3	3	0.06	0.94
10	0.710915	0.712989	0.29	1.00	3	4	0.06	0.94
11	0.723233	0.723803	0.08	1.00	5	2	0.03	0.97
12	0.735215	0.736228	0.14	1.00	1	3	0.24	0.76
13	0.743810	0.742689	-0.15	1.00	6	2	0.04	0.96
14	0.764737	0.765836	0.14	1.00	7	3	0.19	0.81
15	0.781507	0.781524	0.00	1.00	2	3	0.14	0.86
16	0.804756	0.802060	-0.33	1.00	5	3	0.00	1.00
17	0.804756	0.805306	0.07	1.00	8	3	0.12	0.88
18	0.851238	0.853570	0.27	1.00	4	3	0.10	0.90
19	0.852772	0.857640	0.57	1.00	6	3	0.01	0.99
20	0.857761	0.859140	0.16	1.00	5	4	0.44	0.56
21	0.866904	0.865500	-0.16	1.00	7	4	0.17	0.83
22	0.868618	0.867118	-0.17	1.00	6	4	0.34	0.66
23	0.869927	0.868664	-0.15	1.00	1	4	0.13	0.87
24	0.885220	0.887493	0.26	1.00	2	4	0.15	0.85
25	0.891891	0.889768	-0.24	1.00	8	4	0.17	0.83
26	0.909537	0.905829	-0.41	1.00	1	5	0.17	0.83
27	0.916295	0.917161	0.09	1.00	7	5	0.18	0.82
28	0.919592	0.921527	0.21	1.00	6	5	0.08	0.92
29	0.927857	0.922762	-0.55	1.00	5	5	0.32	0.68
30	0.959310	0.959341	0.00	1.00	4	4	0.01	0.99
31	0.969417	0.964602	-0.50	1.00	6	6	0.27	0.73
32	0.980061	0.978085	-0.20	1.00	2	5	0.09	0.91
33	0.992954	0.989705	-0.33	1.00	8	5	0.09	0.91
34	1.047186	1.050417	0.31	1.00	1	6	0.06	0.94
35	1.062793	1.064885	0.20	1.00	4	5	0.11	0.89
36	1.069153	1.071688	0.24	1.00	7	6	0.06	0.94
37	1.076250	1.078840	0.24	1.00	3	5	0.08	0.92
38	1.086361	1.088590	0.21	1.00	5	6	0.16	0.84
39	1.089420	1.092253	0.26	1.00	5	7	0.68	0.32
40	1.131440	1.135363	0.35	1.00	5	8	0.18	0.82
41	1.135743	1.136634	0.08	1.00	2	6	0.10	0.90
42	1.140723	1.142427	0.15	1.00	1	7	0.10	0.90
43	1.142958	1.143087	0.01	1.00	8	6	0.10	0.90
44	1.144497	1.144722	0.02	1.00	7	7	0.10	0.90

Bulk Modulus= 0.586

c11	c22	c33	c23	c13	c12	c44	c55	c66
1.0139	1.0139	1.0139	0.3724	0.3724	0.3724	0.3208	0.3208	0.3208

```
     d1       d2       d3
 0.15930  0.16441  0.25696

 loop# 5  rms error=  0.2925 %, changed by -.0000012 %

 length of gradient vector=  0.000000  blamb=  0.000000

 eigenvalues          eigenvectors
     0.43145   1.00 0.04
   158.53170  -0.04 1.00

chisquare increased 2% by the following % changes in independent parameters
  0.58 -0.08
  0.00  0.09
```

Tb6FeBi2 - B3 - 1T - .0576 gm - 300K
free moduli are c11, c44
using 10 order polynomials mass= 0.0576 gm rho= 9.302 gm/cc

n	fex	fr	%err	wt	k	i	df/d(moduli)	
1	0.329512	0.327009	-0.76	0.00	4	1	0.00	1.00
2	0.394955	0.395212	0.07	1.00	1	2	0.20	0.80
3	0.405422	0.405816	0.10	1.00	7	2	0.20	0.80
4	0.552380	0.554957	0.47	1.00	5	1	0.14	0.86
5	0.572511	0.575180	0.47	1.00	8	2	0.04	0.96
6	0.591788	0.592657	0.15	0.00	2	2	0.05	0.95
7	0.617257	0.614411	-0.46	1.00	4	2	0.00	1.00
8	0.646494	0.643385	-0.48	1.00	3	2	0.02	0.98
9	0.688537	0.687245	-0.19	1.00	3	3	0.07	0.93
10	0.747241	0.752289	0.68	1.00	3	4	0.05	0.95
11	0.756336	0.757306	0.13	1.00	1	3	0.23	0.77
12	0.756619	0.759258	0.35	1.00	5	2	0.04	0.96
13	0.781227	0.782753	0.20	1.00	6	2	0.05	0.95
14	0.803434	0.803113	-0.04	1.00	2	3	0.13	0.87
15	0.814925	0.814565	-0.04	1.00	7	3	0.11	0.89
16	0.840433	0.845240	0.57	1.00	5	3	0.01	0.99
17	0.846376	0.846201	-0.02	1.00	8	3	0.06	0.94
18	0.880133	0.884072	0.45	1.00	6	3	0.01	0.99
19	0.888030	0.884515	-0.40	1.00	4	3	0.11	0.89
20	0.888841	0.892173	0.37	1.00	1	4	0.15	0.85
21	0.893979	0.893775	-0.02	1.00	7	4	0.25	0.75
22	0.903242	0.896021	-0.80	1.00	2	4	0.16	0.84
23	0.909149	0.910058	0.10	1.00	5	4	0.42	0.58
24	0.911913	0.910367	-0.17	1.00	8	4	0.22	0.78
25	0.923560	0.922182	-0.15	1.00	6	4	0.28	0.72

```
 26 0.940802 0.937627 -0.34 1.00 1 5 0.17 0.83
 27 0.948814 0.950526  0.18 1.00 6 5 0.10 0.90
 28 0.971051 0.965689 -0.55 1.00 4 4 0.01 0.99
 29 0.974506 0.967146 -0.76 1.00 7 5 0.17 0.83
 30 0.981712 0.972915 -0.90 0.00 5 5 0.30 0.70
 31 1.018008 1.013810 -0.41 1.00 6 6 0.27 0.73
 32 1.024120 1.021164 -0.29 1.00 2 5 0.09 0.91
 33 1.050021 1.044022 -0.57 1.00 8 5 0.10 0.90
 34 1.081284 1.080466 -0.08 1.00 1 6 0.06 0.94
 35 1.087536 1.092357  0.44 1.00 4 5 0.09 0.91
 36 1.105502 1.110322  0.44 1.00 3 5 0.08 0.92
 37 1.122074 1.121465 -0.05 1.00 7 6 0.05 0.95
 38 1.122074 1.122455  0.03 1.00 5 6 0.15 0.85
 39 1.136830 1.142027  0.46 1.00 5 7 0.49 0.51
 40 1.164027 1.166135  0.18 1.00 5 8 0.21 0.79
 41 1.177040 1.176692 -0.03 1.00 2 6 0.08 0.92
 42 1.189963 1.192494  0.21 1.00 8 6 0.08 0.92
 43 1.203907 1.202849 -0.09 1.00 1 7 0.09 0.91

Bulk Modulus=      0.591

   c11      c22      c33      c23      c13      c12      c44      c55      c66
 1.0164 1.0164 1.0164 0.3776 0.3776 0.3776 0.3194 0.3194 0.3194

      d1       d2       d3
  0.14966  0.15986  0.25882

 loop# 4  rms error=  0.3668 %, changed by -.0000003 %

 length of gradient vector=  0.000001  blamb=  0.000000

 eigenvalues          eigenvectors
      0.28369   1.00 0.04
    150.34613  -0.04 1.00

chisquare increased 2% by the following % changes in independent parameters
  0.86 -0.12
  0.00  0.12.

-------------------------------------------------------------------------------------------------------------------
Tb6FeSb2 - Sample 5 - .2405 gm - 300K
free moduli are  c11, c44
using 10 order polynomials    mass=  0.2405 gm  rho= 8.574 gm/cc

 n     fex      fr    %err wt k i    df/d(moduli)
```

 1 0.264734 0.264220 -0.19 1.00 4 1 0.00 1.00
 2 0.339219 0.338953 -0.08 1.00 4 2 0.00 1.00
 3 0.358479 0.357075 -0.39 1.00 1 2 0.09 0.91
 4 0.377863 0.377722 -0.04 1.00 7 2 0.15 0.85
 5 0.387587 0.387943 0.09 1.00 8 2 0.02 0.98
 6 0.416370 0.416355 0.00 1.00 2 2 0.02 0.98
 7 0.422817 0.422643 -0.04 1.00 6 2 0.11 0.89
 8 0.431171 0.431208 0.01 1.00 1 3 0.40 0.60
 9 0.431532 0.431476 -0.01 1.00 3 2 0.01 0.99
10 0.435730 0.436342 0.14 1.00 5 1 0.01 0.99
11 0.465326 0.465824 0.11 1.00 5 2 0.04 0.96
12 0.467422 0.467330 -0.02 1.00 3 3 0.18 0.82
13 0.484982 0.484790 -0.04 1.00 2 3 0.19 0.81
14 0.491043 0.490918 -0.03 1.00 5 3 0.04 0.96
15 0.514909 0.514564 -0.07 1.00 7 3 0.30 0.70
16 0.527409 0.527653 0.05 1.00 6 3 0.34 0.66
17 0.537768 0.539180 0.26 1.00 3 4 0.02 0.98
18 0.547336 0.544959 -0.43 1.00 8 3 0.19 0.81
19 0.559175 0.558557 -0.11 1.00 5 4 0.44 0.56
20 0.578819 0.578967 0.03 1.00 4 3 0.08 0.92
21 0.580336 0.580139 -0.03 1.00 5 5 0.42 0.58
22 0.583495 0.582600 -0.15 1.00 2 4 0.03 0.97
23 0.588437 0.587887 -0.09 1.00 1 4 0.14 0.86
24 0.595796 0.595580 -0.04 1.00 6 4 0.06 0.94
25 0.598311 0.597519 -0.13 1.00 7 4 0.09 0.91
26 0.629571 0.629432 -0.02 1.00 7 5 0.16 0.84
27 0.629571 0.629677 0.02 1.00 8 4 0.01 0.99
28 0.634315 0.633893 -0.07 1.00 6 5 0.19 0.81
29 0.653277 0.653464 0.03 1.00 1 5 0.06 0.94
30 0.674423 0.674241 -0.03 1.00 6 6 0.12 0.88
31 0.698794 0.699269 0.07 1.00 1 6 0.11 0.89
32 0.701592 0.701996 0.06 1.00 7 6 0.11 0.89
33 0.704340 0.704571 0.03 1.00 1 7 0.10 0.90
34 0.706629 0.707483 0.12 1.00 5 6 1.07-0.07
35 0.716068 0.715531 -0.07 1.00 8 5 0.17 0.83
36 0.724246 0.724161 -0.01 1.00 2 5 0.12 0.88
37 0.752933 0.753738 0.11 1.00 4 4 0.01 0.99
38 0.754988 0.756262 0.17 1.00 3 5 0.08 0.92
39 0.758971 0.761470 0.33 1.00 5 7 0.14 0.86
40 0.769672 0.769734 0.01 1.00 8 6 0.14 0.86
41 0.771879 0.772510 0.08 1.00 2 6 0.15 0.85
42 0.772273 0.773769 0.19 1.00 7 7 0.08 0.92
43 0.786577 0.787099 0.07 1.00 3 6 0.15 0.85
44 0.802178 0.802042 -0.02 1.00 4 5 0.17 0.83
45 0.808191 0.809436 0.15 1.00 6 7 0.08 0.92

Bulk Modulus= 0.615

c11	c22	c33	c23	c13	c12	c44	c55	c66
1.0758	1.0758	1.0758	0.3843	0.3843	0.3843	0.3457	0.3457	0.3457

d1	d2	d3
0.26945	0.30923	0.33663

loop# 8 rms error= 0.1358 %, changed by 0.0000007 %

length of gradient vector= 0.000002 blamb= 0.000000

eigenvalues	eigenvectors	
0.78736	1.00	0.04
143.31290	-0.04	1.00

chisquare increased 2% by the following % changes in independent parameters

0.19	-0.02
0.00	0.04

VITA

David M. McCarthy attended UT Knoxville in the Fall of 2004. He obtained his BS in Materials Science and Engineering. He consequentially enrolled in UT's graduate school the Fall of 2008 in the College of Engineering, Department of Materials Science ang Engineering. He obtained a research assistanceship under Dr. Veerle Keppens to work on magnetostriction and Resonant Ultrasound Spectroscopy. His research transferred into this thesis. His research committee accepted his thesis. He graduated from UT with a MS in Materials Science and Engineering in the Summer of 2010.